Applied Water Science (2026) 16:132
https://doi.org/10.1007/s13201-026-02807-z

ORIGINAL ARTICLE

Valorization of *Ulva fasciata* biowaste incorporated in PVA nanofibers and films membranes: Box-Behnken optimization toward advanced wastewater treatment and blue economy applications

Shimaa Husien[1] · **Waleed I. M. El-azab**[2] · **Hager R. Ali**[2] · **Nour Sh. El-Gendy**[2,3] · **Wael Mamdouh**[1]

Received: 3 July 2025 / Accepted: 17 February 2026 / Published online: 24 March 2026

Abstract

The removal of low-concentration pollutants from wastewater remains a major challenge in advanced treatment processes, where conventional wastewater treatment methods often underperform due to limited mass transfer and weak interaction kinetics. In this study, a novel bio-based membrane system was developed using polyvinyl alcohol (PVA) and *Ulva fasciata* bioethanol byproduct extract (UFBE), a waste-derived material rich in antimicrobial ulvan. Dual-format membranes, comprising nanofibers and films, were fabricated through green electrospinning and solvent-casting techniques using water-based systems. Box-Behnken response surface methodology was employed to optimize the electrospinning parameters for minimized fiber diameter and morphological uniformity. Characterization analyses (SEM, SEM-EDX, FTIR, TGA, XRD, BET, tensile strength, swelling, and solubility tests) confirmed the successful integration of UFBE and improvements in thermal and mechanical properties. The membranes were applied to aged oilfield wastewater representing a low-pollutant treatment challenge. Despite reduced contaminant levels, the membranes achieved nearly 100% oil removal, an 82% reduction in turbidity, and substantial declines in hardness and scaling potential. These findings underscore the membrane's sensitivity, selectivity, and suitability for tertiary treatment applications. This work presents a foundational approach to developing multifunctional, sustainable membranes from algal waste, offering new opportunities for bio-derived materials in environmental remediation.

Keywords Antifouling membrane · Blue economy · Films · Nanofibers · Trace contaminants · Biowaste valorization

Communicated by Zhaoliang Cui

✉ Wael Mamdouh
wael_mamdouh@aucegypt.edu

Shimaa Husien
shimaa.husien@aucegypt.edu

Waleed I. M. El-azab
welazab@yahoo.com

Hager R. Ali
d_hager80@epri.sci.eg

Nour Sh. El-Gendy
nshelgendy@msa.edu.eg; nourepri@yahoo.com

[1] Department of Chemistry, School of Sciences and Engineering (SSE), The American University in Cairo (AUC), AUC Avenue, P.O. Box 74, New Cairo 11835, Egypt

[2] Egyptian Petroleum Research Institute (EPRI), Nasr City 11727, Cairo, Egypt

[3] Center of Excellence, October University for Modern Sciences and Arts (MSA), 6th of October City 12566, Giza, Egypt

Abbreviations

UFBE	Ulva fasciata byproducts extract
PVA	Poly vinyl alcohol
PVA-UFBE	Ulva fasciata byproducts extract encapsulated poly vinyl alcohol
DOE	Design of Experiment

Introduction

Seaweeds, or macroalgae, are fast-growing aquatic organisms with plant-like morphology, capable of reaching lengths up to 60 m (McHugh 2003; Arumugam et al. 2018). In 2018, global seaweed production, including both wild and cultivated sources, reached approximately 32.4 million tons (fresh weight), highlighting their growing role in the blue economy (Buschmann et al. 2017; Action 2020; Ktari et al. 2022). Owing to their unique biochemical composition and structural complexity, seaweeds have been increasingly utilized in environmental applications such as nutrient removal, eutrophication control, and the bioremediation of contaminated aquatic ecosystems (Holdt and Edwards 2014; Kim et al. 2017). Additionally, their exceptional ability to bioaccumulate heavy metals also makes them effective biomonitors and natural scavengers of pollutants (El-Mahrouk et al. 2023). Among these, *Ulva fasciata*, commonly referred to as sea lettuce, is a green macroalga (family: *Ulvaceae*) known for its high tolerance to environmental stress and strong bioaccumulation potential. Its presence often serves as a biological indicator of anthropogenic pollution or freshwater influx in marine ecosystems (Madany et al. 2021; El-Mahrouk et al. 2023). While these characteristics limit its suitability for direct human consumption. *Ulva fasciata* has been increasingly valorized into a range of bioproducts, including salts, lipids, starch, proteins, cellulose, and particularly ulvan, a sulfated polysaccharide with reported antioxidant, antiviral, and antimicrobial activities (Trivedi et al. 2016; El-Gendy et al. 2023). However, the residual biomass generated following such valorization processes remains underutilized, representing both an environmental burden and a missed opportunity for biowaste recovery. Previous studies have demonstrated the feasibility of using *Ulva fasciata* biomass for pollutant adsorption, particularly for dyes and heavy metals in wastewater (Lekshmi et al. 2022; Shoaib, Van et al. 2024). Meanwhile, conventional water treatment methods such as coagulation (Jiang 2015), electrocoagulation (Hashim et al. 2020), adsorption (Yousef et al. 2020), advanced oxidation process (Garrido-Cardenas et al. 2020), biological treatment, and chemical treatment techniques (Saleh et al. 2020) have been widely explored for pollutant removal. Nonetheless, the majority of these technologies have been optimized for the removal of pollutants at moderate to high concentrations, whereas the treatment of residual or trace-level contaminants remains comparatively underexplored (Abdelhamid et al. 2023). This represents a critical research gap, as the removal of dilute pollutants poses distinct challenges due to lower sorption kinetics and limited interaction with active sites at low concentrations (Zinicovscaia 2016). As Sarmah et al. emphasized, addressing this challenge requires materials that exhibit both high surface reactivity and selectivity, capable of functioning under stringent conditions (Sarmah et al. 2006). Advanced membrane filtration systems are increasingly recognized for their potential in polishing and tertiary treatment applications, particularly where low-level contaminant removal is essential to meet tightening regulatory discharge standards. To address this challenge, the present study introduces a novel, dual-format membrane system composed of polyvinyl alcohol (PVA) and UFBE. *Ulva fasciata* bioethanol byproduct extract (UFBE) is a waste-derived material enriched with ulvan, a sulfated polysaccharide with well-documented antimicrobial properties (Paulert et al. 2007; El-Gendy et al. 2023). To the best of the authors' knowledge, this is the first study to report both the fabrication of dual-format membranes from a novel PVA/UFBE composite and their application in the selective removal of low-concentration pollutants from real wastewater. The integration of UFBE not only improves the antifouling and anti-scaling properties of PVA but also reduces its water solubility, particularly after thermal treatment. The membranes were fabricated using green, water-based electrospinning and solvent casting methods in alignment with circular economy principles. Box-Behnken response surface methodology was employed to optimize electrospinning parameters, yielding uniform nanofibers with minimized diameters. The membranes were tested on real oilfield wastewater, aged for three months to reflect a challenging, low-pollutant scenario. Thus, this study serves as a foundational contribution at the intersection of material science, environmental engineering, and biowaste valorization. It paves the way for a new class of sustainable, multifunctional membranes for advanced wastewater treatment applications.

Materials and methods

Extract preparation

The green macroalgae *Ulva fasciata* biomass applied in this study is the spent waste disposed of bioethanol production process used in the study performed by El-Gendy, et al. (El-Gendy et al. 2023). The *Ulva fasciata* byproducts (UFB) were further extracted using water extraction method (Plaza et al. 2010) where 1 gm of UFB was mixed with 10 ml dist. H_2O and left to boil at 150 °C for 20 min. After that, the algae solution was filtered, and the extract was separated into a clean flask. The extraction method was repeated two times to obtain a full process of three multi-extraction method. The extract was dried using lyophilizer to obtain the powder of *Ulva fasciata* by-products extract (UFBE).

Electrospinning solution preparation

The electrospinning solution was prepared using polyvinyl alcohol (PVA, ~125,000 g/mol molecular weight; Sigma-Aldrich) at a concentration of 10% w/v. Initially, the UFBE powder was dispersed in distilled water using probe sonication to ensure uniform suspension. Following dispersion, PVA powder was gradually added to the UFBE solution in a closed flask and heated to 120 °C under continuous stirring for 2 h to ensure complete dissolution. The resulting solution was then maintained under constant stirring at 500 rpm at room temperature overnight to ensure homogeneity prior to electrospinning. Various concentrations of UFBE were evaluated and optimized using Box-Behnken response surface methodology (RSM) via Design-Expert® software.

Nanofibers optimization and characterization

A Box-Behnken response surface methodology (RSM) design was employed to optimize three key electrospinning parameters: UFBE concentration (mg/mL), flow rate (mL/h), and applied voltage (kV). The experimental design consisted of 15 runs, as shown in Table 1S, all conducted at a fixed polyvinyl alcohol (PVA) concentration of 10% w/v and a constant distance of 16 cm between the needle tip and the collector. Each run was electrospun to produce nanofiber membranes for morphological analysis. The morphology and diameter of the fabricated nanofibers were characterized using field emission scanning electron microscopy (FESEM; Leo Supra 55, Zeiss Inc., Germany). Prior to imaging, the samples were sputter-coated with gold at 10 mA for 6 min. SEM micrographs were captured at magnifications of ×2,000 and ×10,000. Fiber diameters were measured using ImageJ software, with approximately 100 fibers quantified per image to ensure statistical reliability. The resulting data were processed using OriginPro® 19 for graphical analysis and average diameter calculation. Optimization analysis was then performed using Design-Expert® software to determine the optimal electrospinning parameters for minimal fiber diameter and uniform morphology, as detailed in Table 1.

Table 1 Design Matrix of the response surface model

Std	Run	Factor 1	Factor 2	Factor 3	Response 1
		A: UFBE concentration	B: Flow rate	C: Voltage	Diameter
		mg/ml	ml/hr.	mV	nm
5	1	1.5	0.75	18	142.38
10	2	2	1	18	163.21
11	3	2	0.5	22	161.14
13	*4*	*2*	*0.75*	*20*	*174.16*
6	5	2.5	0.75	18	152.03
14	*6*	*2*	*0.75*	*20*	*173.69*
9	7	2	0.5	18	209.67
1	**8**	**1.5**	**0.5**	**20**	**109.31**
2	**9**	**2.5**	**0.5**	**20**	**107.07**
4	10	2.5	1	20	135.64
3	11	1.5	1	20	130.07
8	12	2.5	0.75	22	160.18
7	13	1.5	0.75	22	166.48
12	14	2	1	22	245.52
15	*15*	*2*	*0.75*	*20*	*175.39*

Optimum run application in nanofibers and films preparation

The optimal parameters identified through the Design Expert response optimizer were applied for electrospinning to validate the optimization results. The same optimal formulation was also used for film preparation via the solvent casting method. Specifically, films were prepared using 10% (w/v) PVA, approximately 2.49 mg/mL UFBE powder, and a casting volume of 5 mL. Both the PVA-UFBE nanofibers and films underwent heat treatment at 155 °C for 1 h to reduce the water solubility of PVA. Swelling and solubility behavior of the membranes were assessed before and after heat treatment following 48 h of immersion in distilled water. The initial dry weight (W_1) was recorded, followed by weighing after water immersion and removal (W_2). Samples were then oven-dried at 60 °C until constant weight (W_3). Swelling and solubility were calculated using Eq. 1 and 2, respectively (Kuchaiyaphum et al. 2013). The resulting data were analyzed and are presented in the results Sect.

$$Swelling\ (\%) = \frac{W_2 - W_1}{W_1} * 100 \tag{1}$$

$$Solubility\ (\%) = \frac{W_1 - W_3}{W_1} * 100 \tag{2}$$

PVA-UFBE nanofibers and films characterization

The prepared nanofiber meshes, including PVA-UFBE nanofibers and films, PVA-only nanofibers and films (as control), and UFBE powder, were characterized using various analytical techniques. Surface morphology was examined via scanning electron microscopy (SEM; FESM, Leo Supra 55, Zeiss Inc., Germany) as detailed in Sect. Nanofibers optimization and characterization. Additionally, the cross-sections of the PVA and PVA-UFBE films were prepared by cutting the membranes into two pieces under nitrogen conditions. The exposed surfaces were then gold-sputtered at 10 mA for 6 min before imaging, and the cross-sectional morphology was subsequently visualized using SEM (Neoscope JCM-6000 Plus, JEOL). Chemical structure and functional groups were analyzed using Fourier Transform Infrared Spectroscopy (FT-IR; Thermo Scientific Nicolet 8700, USA). The KBr pellet method was employed for UFBE powder, while nanofiber and film samples were directly analyzed across a wavenumber range of 4000–400 cm⁻¹. Thermal stability was assessed using thermogravimetric analysis (TGA; TGA Q50, AUC). Approximately 5 mg of each sample was placed in aluminum crucibles and heated from room temperature to 600 °C at a rate of 10 °C/min for 76 min. Differential thermogravimetric (DTG) data were derived from the TGA results based on mass loss rate (da/dt) versus temperature. Both TGA and DTG profiles were plotted and discussed in the results section. X-ray diffraction (XRD) analysis was conducted using an Advanced X-ray solutions instrument to identify the crystalline structure of the nanofibers: UFBE powder, PVA nanofiber, PVA-UFBE nanofiber, PVA film, and PVA-UFBE film composites. Data were collected using Cu Kα radiation with a Ni filter under operating conditions of 40 kV and 30 mA. Pore characteristics of the PVA-UFBE nanofibers and films were evaluated using the Brunauer–Emmett–Teller (BET) method with a Micromeritics ASAP 2020 analyzer under nitrogen adsorption at 150 °C for 12 h. Mechanical properties were assessed using a universal testing machine (Instron 5569 Load Frame, USA) with a 5 kN load cell. Samples were cut into dumbbell shapes (36 × 8 mm) following ASTM D882 standards, with a gauge length of 10 mm. Sample thicknesses were 0.075, 0.070, 0.014, and 0.090 mm for PVA nanofibers, PVA-UFBE nanofibers, PVA films, and PVA-UFBE films, respectively. Tensile strength values were recorded and analyzed.

Wastewater treatment and analysis

The prepared PVA-UFBE nanofiber and film membranes were evaluated for their filtration performance using a real formation water sample collected from the outlet of an API separator at an Egyptian oil field located in the Gulf of Suez region. To simulate a realistic and challenging treatment scenario, the wastewater sample was stored under ambient laboratory conditions for approximately three months prior to filtration. This aging period allowed for partial natural degradation of labile pollutants, resulting in a diluted matrix of low-concentration residual contaminants. Such conditions are representative of tertiary or polishing treatment stages, where pollutant removal becomes increasingly difficult due to diminished concentration gradients and interaction kinetics. The filtration process was carried out using five different membrane types: PVA nanofiber, PVA-UFBE nanofiber, PVA film, PVA-UFBE film, and a commercial-grade filter paper (as a reference). A 50 mL volume of the aged wastewater was filtered through each membrane type, and comprehensive water quality analysis was conducted on both untreated and treated samples. Water quality parameters were determined according to standardized protocols. Total suspended solids (TSS) and total dissolved solids (TDS) were measured following ASTM D5907. Salinity was assessed using the APHA Method 2520. Alkalinity species, including carbonate (CO_3^{2-}), bicarbonate (HCO_3^-), and hydroxide (OH^-), were quantified in accordance with ASTM D3875. Water hardness (Ca^{2+} and Mg^{2+}) was measured per ASTM D6919 and calculated as per ASTM D1126. Density and specific gravity were determined using a digital density meter (Anton Paar DMA 4101) according to ASTM D4052. pH was measured using a calibrated digital pH meter (Toledo SevenGo) as specified in ASTM D1293. Electrical conductivity and resistivity were evaluated using a digital conductivity meter (WTW 330i) following ASTM D1125. Ion concentrations were analyzed using ion chromatography (Dionex™ ICS-6000 Capillary HPIC™ System), employing AS9 and CS12 columns for anion and cation determination, respectively, according to ASTM D4327 and ASTM D6919. Heavy metal concentrations were measured via flame atomic absorption spectroscopy (AAS) using an Analytik Jena ZEEnit 700P, as per ASTM D4691. Finally, scaling tendency before and after treatment was assessed using OLI ScaleChem® software version 4.1 (OLI Systems Inc., Morris Plains, NJ, USA). Simulations were conducted under representative field conditions: flow rate of 1000 barrels per day, temperature of 25 °C, and pressure of 1 bar.

Results and discussion

The prepared nanofibers optimization results

The morphology of the 15 nanofiber meshes prepared through the response surface methodology (RSM) was characterized using field-emission scanning electron microscopy (FE-SEM). Representative micrographs for each run are presented in Figs. 1S, 2, 3, 4, 5, 6, 7, 8, 9, 10, 11, 12, 13, 14 and 15S. Nanofiber diameters were quantitatively analyzed using ImageJ software, and data visualization was performed using OriginPro® 2019. The resulting fiber diameter values were further analyzed using Design-Expert software to determine the optimal processing parameters that minimize fiber diameter and eliminate bead formation. FE-SEM analysis revealed bead formation in most fibers, particularly in runs 2, 3, 4, 5, 6, 7, 10, 12, 13, 14, and 15 (Figs. 2S, 3S, 4S, 5S, 6S, 7S, 10S, 12S, 13S and 14S, and 15S). In contrast, nanofibers from runs 1, 8, 9, and 11 (Figs. 1S, 8S and 9S, and 11S) exhibited uniform, bead-free structures. Notably, runs 8 and 9, which utilized UFBE concentrations of 1.5 mg/mL and 2.5 mg/mL, respectively, achieved the smallest fiber diameters (~ 109 nm and ~ 107 nm) without bead formation. These findings highlight the critical influence of flow rate (0.5 mL/h) and applied voltage (20 kV) in achieving uniform nanofiber morphology. To validate the robustness of the optimized conditions, three additional runs (runs 4, 6, and 15) were performed. The fiber diameters obtained from these validation runs were consistent and demonstrated minimal bead formation, supporting the predictive accuracy of the response surface model (see Fig. S4, S6, S15 and Table 1).

Statistical analysis and fitting of the applied response surface model

The statistical analysis was applied using multiple regression analysis, quadratic model was stated by the response surface analysis result by using design expert software. ANOVA analysis assesses the significance of the main and interacting effects of the three parameters of the study design (UFBE concentration, flow rate, and voltage) on the diameter and morphology of the nanofiber. The box Behnken design matrix, including the results of the nanofiber's diameter, is shown in Table 1. In Table 2 ANOVA analysis, a P-value less than 0.05 suggests the significance of the model parameters, whereas a P-value higher than 0.05 refers to the non-significant parameters. Accordingly, Table 2 results suggested that B, C, AC, BC, A^2, B^2, and C^2 are significant model terms, while the other parameters with P-values higher than 0.05 are non-significant. Furthermore, results suggested that the quadratic model is the best-fit model, and it has an insignificant lack of fit with a P-value of 0.1247 relative to the pure error with an F-value of 7.18. However, there is a 12.47% chance that a lack of fit F-value this large could occur due to noise. Generally, a non-significant lack of fit indicates that the mathematical model effectively represents the experimental data. Moreover, Fig. 1 compares the actual average diameter of the prepared PVA-UFBE nanofibers and the predicted diameter by the RSM model. According to the data in Fig. 1, there is an agreement between the actual and the predicted coded factors of the RSM model with an R^2 of nearly 0.999. The predicted R^2 result is 0.984, which is considered a reasonable value because it is close to the adjusted R^2 value of 0.997; the difference is less than 0.2. Furthermore, the Adeq. Precision indicated adequate signal because its value is 89,013, which is larger than 4, which states the applicability of this model to investigate the design space.

Coefficient of coded variables

The coefficient results express the expected change in the response per unit change in factor value when all remaining factors are held constant. The intercept in an orthogonal design is the overall average response of all runs. The coefficients are adjusted around that average based on the factor settings. When the factors are orthogonal the VIFs are 1; VIFs greater than 1 indicate multi-collinearity, the higher the VIF the more severe the correlation of factors. As a rough rule, VIFs less than 10 are tolerable, See Table 2S. Generally, the final equation in terms of coded factors is expressed in Eq. 3. The equation can be applied to make predictions about the response for given levels of each factor. By default, the high levels of the factors are coded as + 1 and the low levels are coded as -1 as in Table 1S. The coded equation is useful for identifying the relative impact of the factors by comparing the factor coefficients.

$$\begin{aligned}\text{Diameter} = {} & +174.41 + 0.8339\text{A} + 10.91\text{B} \\ & + 8.26\text{C} + 1.95\text{AB} - 3.99\text{AC} + 32.71\text{BC} \\ & - 46.75\text{A}^2 - 7.14\text{B}^2 + 27.61\text{C}^2\end{aligned} \tag{3}$$

whereas the equation in terms of actual factors, Eq. 4 can be displayed to predict the response for each factor-specific level. However, this equation could not be used to determine the relative impact of each factor because the coefficients are scaled to accommodate the units of each factor, and the intercept is not at the center of the design space.

$$\begin{aligned}\text{Diameter} = {} & +2849.78221 + 817.74940\ \text{UFBE concentration} \\ & - 1124.73145\ \text{flow rate}\ 313.06541\text{voltage} \\ & + 15.62076\ \text{UFBE concentration} * \text{flow rate} \\ & - 3.98704\ \text{UFBE concentration} * \text{Voltage} \\ & + 65.42324\ \text{flow rate} * \text{voltage} - 187.01406\ \text{UFBE concentration}^2 \\ & - 114.23102\ \text{flow rate}^2 + 6.90251\ \text{voltage}^2\end{aligned} \tag{4}$$

Table 2 Analysis of variance (ANOVA) of the response surface mathematical quadratic model for fiber diameter

Source	Sum of squares	df	Mean square	F-value	*p*-value	
Model	17674.19	9	1963.80	542.61	< 0.0001	Significant
A- UFBE concentration	5.56	1	5.56	1.54	0.2700	
B-Flow rate	951.72	1	951.72	262.96	< 0.0001	
C-Voltage	545.38	1	545.38	150.69	< 0.0001	
AB	15.25	1	15.25	4.21	0.0953	
AC	63.59	1	63.59	17.57	0.0086	
BC	4280.20	1	4280.20	1182.64	< 0.0001	
A^2	8070.98	1	8070.98	2230.05	< 0.0001	
B^2	188.20	1	188.20	52.00	0.0008	
C^2	2814.70	1	2814.70	777.72	< 0.0001	
Residual	18.10	5	3.62			
Lack of fit	16.56	3	5.52	7.18	0.1247	Not significant
Pure error	1.54	2	0.7685			
Cor total	17692.29	14				

R^2 0.9990, Adjusted R^2 0.9971, Predicted R^2 0.9848

Fig. 1 Actual vs. predicted RSM-responses of nanofibers diameter

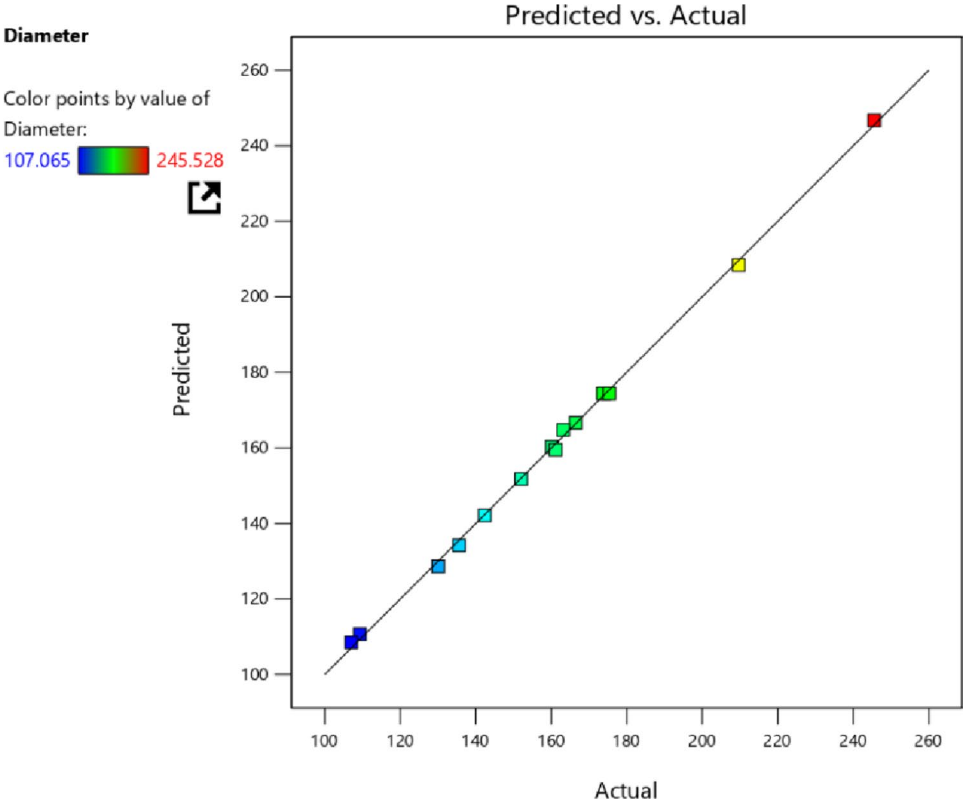

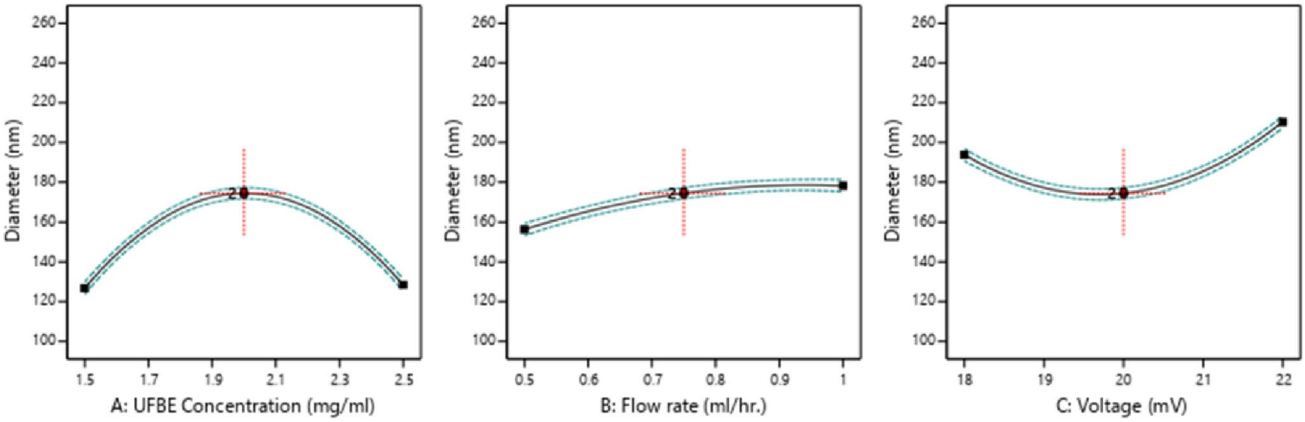

Fig. 2 Main effects of RSM for the various parameters (algae concentration, flow rate, voltage) effect of fiber diameter

Effect of processing factors on nanofibers diameter response

The influence of processing parameters on nanofiber diameter was analyzed using the main effects plot (Fig. 2), and statistical output (Table 2). Among the studied variables, the concentration of *Ulva fasciata* bioethanol byproduct extract (UFBE, Factor A) was found to have no statistically significant effect on fiber diameter ($p > 0.05$). In contrast, both flow rate (Factor B) and applied voltage (Factor C) demonstrated significant effects ($p < 0.05$). The model predicted an optimal UFBE concentration at both the lower and higher bounds of 1.5 and 2.5 mg/mL, further confirming the minimal influence of this factor on fiber morphology. This is attributed to the consistent dispersion behavior of the UFBE within the polymer matrix, which does not notably interfere with solution viscosity or electrostatic response under the examined conditions. A strong correlation was observed between increased flow rate and increased fiber diameter. Higher flow rates result in a greater volume of polymer solutions being dispensed, which reduces the ability of the applied voltage to stretch and elongate the jet effectively. Therefore, a flow rate of 0.5 mL/h was identified as optimal for producing finer fibers. This observation aligns with prior findings, which explain that at a constant voltage, lower flow rates allow for more efficient fiber stretching due to a controlled jet volume and sufficient electrostatic force for elongation. Conversely, higher flow rates lead to bulkier jets that resist elongation, thereby yielding larger fiber diameters due to inadequate ion availability for charge repulsion and fiber thinning (Zargham et al. 2012). Regarding the effect of applied voltage, increasing the voltage from 18 to 20 kV resulted in a reduction in fiber diameter. However, beyond 20 kV, further increases in voltage led to a rise in fiber diameter. This non-linear behavior is consistent with established electrospinning theory: higher voltage initially increases the stretching force on the solution jet, reducing fiber diameter. However, excessively high voltages (critical voltage) shorten the flight time of the jet and destabilize the whipping motion, often leading to bead formation or thicker, less uniform fibers (Deitzel et al. 2001). Thus, an applied voltage of 20 kV was considered optimal for achieving finer, more uniform nanofibers (Ziabari et al. 2010). The present findings agree with previous studies on electrospun nanofibers regarding the influence of flow rate and voltage on fiber morphology. For instance, Bhardwaj and Kundu demonstrated that decreasing the flow rate leads to finer fibers due to enhanced elongation under stable jet formation, whereas higher flow rates hinder stretching and lead to thicker, bead-prone fibers (Yuan et al. 2004; Bhardwaj and Kundu 2010). Similarly, studies by Lee et al. and Huang et al. demonstrated that the applied voltage influences both the initiation and stability of the Taylor cone, where moderate voltage levels produce thinner fibers, but excessive voltage causes instability and increased diameter due to jet disruption (Huang et al. 2003; Lee et al. 2003). Collectively, these results confirm that while additive concentration plays a minimal role in morphological control, the fine-tuning of flow rate and voltage remains critical for tailoring fiber diameter. The present study contributes novel insight by applying this optimization framework to a bio-derived composite system incorporating algal waste, adding to the limited literature on green nanofiber fabrication.

Contour and 3D plots

The interaction effects between selected electrospinning parameters were further evaluated using Box-Behnken response surface methodology (RSM) to determine their combined influence on nanofiber diameter. Specifically, the interactions between UFBE concentration and applied voltage (A×C), as well as flow rate and applied voltage (B×C), exhibited statistically significant effects in the model and contributed positively to reducing fiber diameter. These interactions were visualized using both contour and three-dimensional (3D) surface plots (Figs. 3 and 4). Figure 3a and b illustrate the 3D and contour plots for the A×C interaction. The results indicate that at a UFBE concentration of approximately 1.5 mg/mL and an applied voltage of 18 kV, with the flow rate fixed at 0.75 mL/h, the nanofiber diameter was minimized to approximately 142 nm. This region represents a favorable balance where the presence of bioactive extract and moderate electric field strength enable efficient jet elongation without compromising fiber uniformity. The results observed in the contour plot (Fig. 3a) were further confirmed by the corresponding 3D surface plot (Fig. 3b), demonstrating a clear synergistic effect between UFBE concentration and voltage. Similarly, the interaction between flow rate and voltage (B×C) was explored and visualized in Fig. 4a and b. The contour plot (Fig. 4a) suggests that a lower flow rate of approximately 0.5 mL/h, combined with a higher voltage of 22 kV, and with UFBE concentration fixed at 2 mg/mL, results in fiber diameters around 161 nm. This outcome is corroborated by the 3D surface plot (Fig. 4b), which confirms the favorable interaction of these parameters in producing thinner nanofibers. The improved stretching observed under high voltage and low flow rate conditions aligns with electrospinning theory, as the electric field provides sufficient charge density to elongate the reduced-volume jet, enhancing fiber uniformity and reducing diameter. These findings are consistent with existing literature reporting that the synergistic control of voltage and flow rate is critical to achieving optimized nanofiber dimensions. For instance, studies have shown that while voltage increases jet acceleration and thinning, excessive voltage combined with high flow rates can destabilize the Taylor cone and increase fiber diameter due to premature solidification or jet instability (Baščarević et al. 2024). The observed interactions in this study demonstrate that fine-tuning these parameters is particularly important when incorporating natural extracts like UFBE, whose effects may otherwise be masked in single-factor analysis.

Confirmation test and preparing the optimum nanofiber and films

The optimum parameters that achieve lower fiber diameter were predicted by the response surface model as shown in Fig. 5. The graph shows that by applying 2.49 mg/ml UFBE concentration into 10% PVA with a flow rate of 0.5, and voltage of around 20.9, a nanofiber diameter rate of 103.671 nm could be obtained with 1 degree of desirability. The nanofiber solution and electrospinning process were performed according to the optimum parameters, resulting in a nanofiber diameter of approximately 133 nm. Furthermore, the optimum electrospinning solution was used to form films using the solvent evaporation technique to form PVA-UFBE film. The final obtained membranes after the preparation of

Fig. 3 Contour and 3D plots of the interaction AC between algae concentration and Voltage rate: **a** contour plot, **b** 3D plot

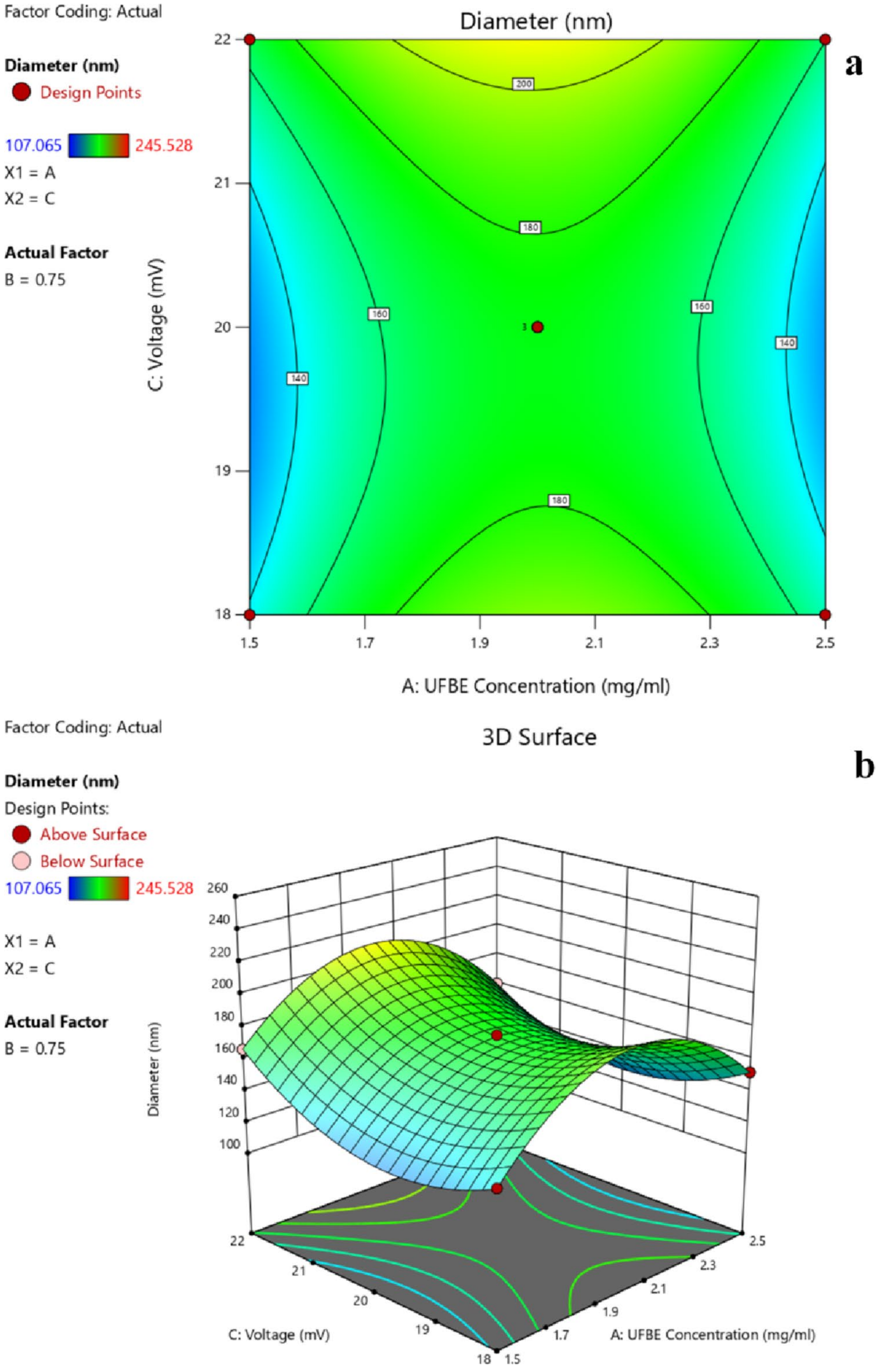

Fig. 4 Contour and 3D plots of the interaction BC between flow rate and voltage rate: **a** contour plot, **b** 3D plot

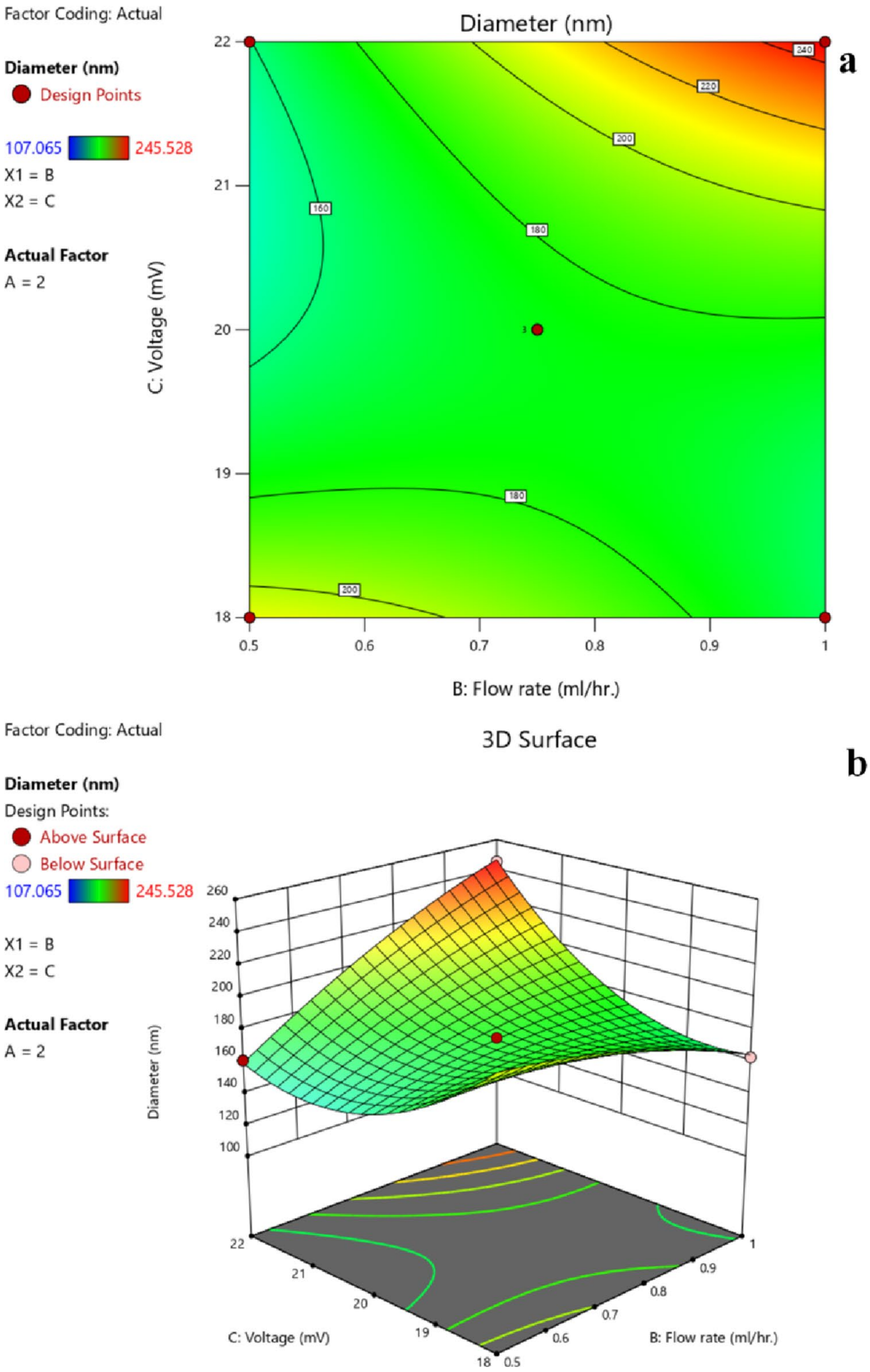

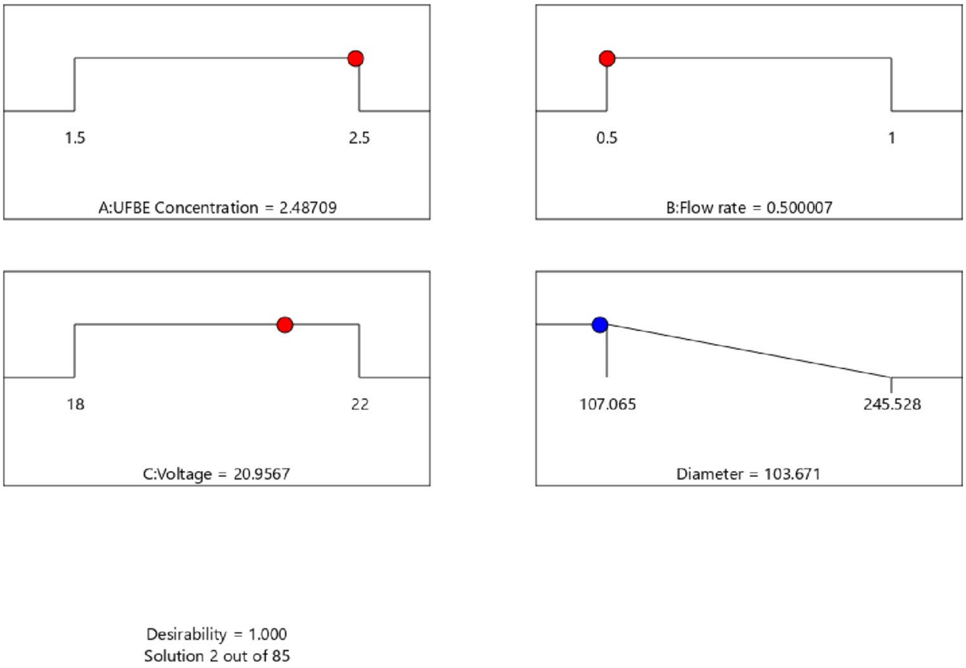

Fig. 5 Predicted RSM optimized parameters that achieve optimum nanofiber diameter response

controls were PVA nanofiber, PVA-UFBE nanofibers, PVA film, and PVA-UFBE film.

Optimum nanofibers and film characterization results

The prepared membranes PVA nanofiber, PVA-UFBE nanofibers, PVA film, and PVA-UFBE film in addition to the UFBE powder were characterized using swelling, solubility, SEM, FT-IR, TGA, BET, and tensile strength analysis.

Fourier transform-Infrared (FT-IR) analysis

FT-IR analysis was performed to examine the chemical structure and functional groups, confirming the successful incorporation of UFBE into the PVA matrix across different material forms, including nanofibers, films, and powders. The spectra for PVA powder, UFBE powder, PVA nanofibers, PVA-UFBE nanofibers, PVA film, and PVA-UFBE film are presented in Fig. 6. The FT-IR spectrum of pure PVA powder displayed characteristic absorption bands at 3437 cm^{-1} (O–H stretching), 2924 and 2852 cm^{-1} (C–H asymmetric and symmetric stretching of alkyl groups), 2361 cm^{-1} (C≡C stretching), 1722 cm^{-1} (C=O stretching), 1637 cm^{-1} (H–O–H bending due to absorbed water), 1462 cm^{-1} (CH_2 bending), 1147 and 1097 cm^{-1} (C–O stretching), and 858 cm^{-1} (C–C skeletal stretching). These bands align well with previously reported spectra for PVA, confirming the polymer's structural integrity (Jipa et al. 2012). The UFBE powder spectrum exhibited prominent bands at 3484 cm^{-1} (O–H stretching from polysaccharides), a weak shoulder at 2992 cm^{-1} (aliphatic C–H stretching characteristic of sugar-based polysaccharides), and a band at 1645 cm^{-1} (O–H bending). Additional peaks at 1417 cm^{-1} (COO^- stretching), 1115 and 995 cm^{-1} (C–O stretching), and 617 cm^{-1} (pyranose ring vibrations) were also observed. These peaks are consistent with ulvan-rich algal polysaccharides, as previously documented in several studies (Karwasra et al. 2017; Chen et al. 2021; Madany et al. 2021; Ibrahim et al. 2022; El-Gendy et al. 2023). The FT-IR spectra of the PVA and PVA-UFBE nanofiber membranes showed typical PVA peaks with some notable shifts due to UFBE incorporation. A broad absorption band around 3336 cm^{-1} corresponds to O–H stretching, indicative of strong intra- and intermolecular hydrogen bonding. Peaks at 2939 cm^{-1} were assigned to –CH_2 asymmetric and symmetric stretching, while 1711 cm^{-1} corresponded to C=O stretching. Additional characteristic peaks appeared at 1421 cm^{-1} (CH–OH bending), 1335 cm^{-1} (C–H and O–H bending), 1265 cm^{-1} (C–H stretching), 1093 cm^{-1} (acetal –C–O–C– linkage), and 850 cm^{-1} (C–C stretching). Importantly, while the band near 1651 cm^{-1} appears in all spectra due to O–H bending present in both PVA and UFBE, it cannot uniquely confirm encapsulation. Instead, incorporation is best substantiated by increased intensity and bandwidth in this region, together with new or amplified peaks unique to UFBE. Notable examples include COO^- stretching (1417 cm^{-1}), which is significantly enhanced in the composite materials, and the acetal C–O–C linkage at 1093 cm^{-1}, with further contributions from pyranose ring vibrations near 617 cm^{-1}. These features are more pronounced in PVA-UFBE nanofibers and films compared to pure PVA, aligning with prior reports of ulvan composite formation (Paipitak

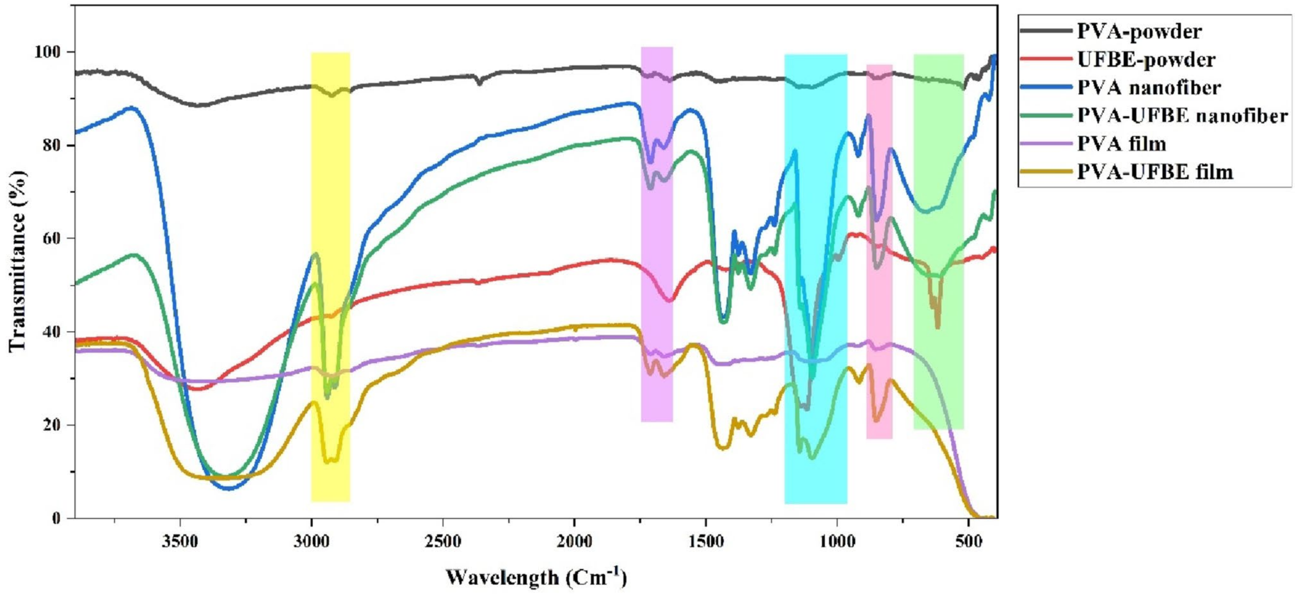

Fig. 6 FT-IR analysis of the different samples prepared

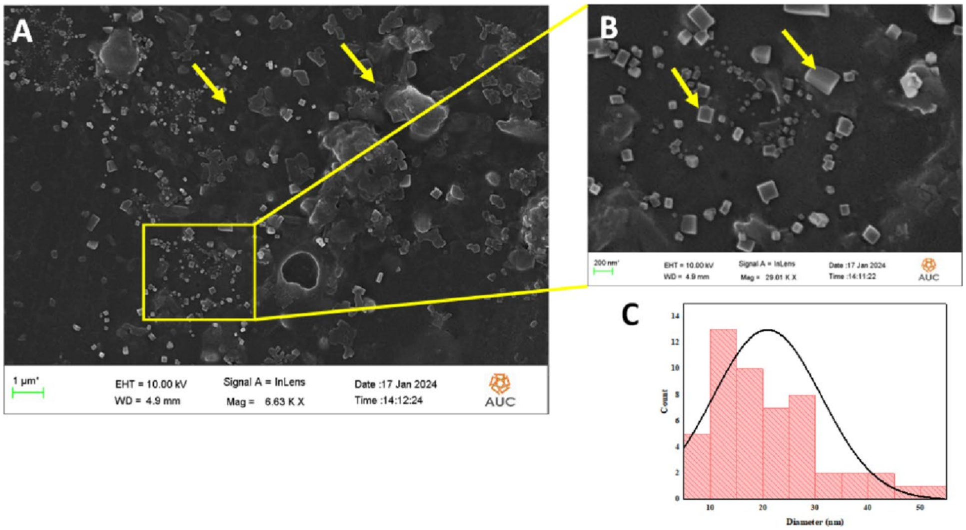

Fig. 7 FE-SEM analysis of the UFBE powder form (**A**) 1 µm magnification cross section (**B**) 200 nm magnification cross section (**C**) Histogram indicating the average diameter of the extract powder (Yellow arrows refers to the UFBE crystal structure)

et al. 2011; Choo et al. 2016; Delan et al. 2022). The cast films (purple and yellow) closely follow the spectral features observed in nanofiber membranes, reflecting stable molecular composition irrespective of fabrication method (electrospinning vs. solvent casting). The observed spectral modifications, including intensity enhancements and peak broadening, confirm UFBE's effective encapsulation in PVA matrices, with no significant chemical degradation or transformation throughout processing. Together, the IR data and their interpretation not only corroborate the incorporation of UFBE into PVA nanofiber and film membranes but also illustrate the molecular signatures associated with hybrid formation.

Scanning electron microscope analysis

Field Emission Scanning Electron Microscopy (FE-SEM) was utilized to investigate the surface morphology of the prepared UFBE powder, as well as the fabricated membranes including PVA nanofibers, PVA-UFBE composite nanofibers, PVA film, and PVA-UFBE film, as illustrated in Figs. 7, 8, 9 and 10. Figure 7 presents the SEM micrograph of the UFBE powder, revealing a non-uniform amorphous structure with irregular, rough surface textures. These morphological features are consistent with the characteristics of sulfated polysaccharide-based algae powders reported by El-Gendy et al. (El-Gendy et al. 2023), where similar biopolymers displayed non-crystalline morphology due to the heterogeneous composition of ulvan. ImageJ and

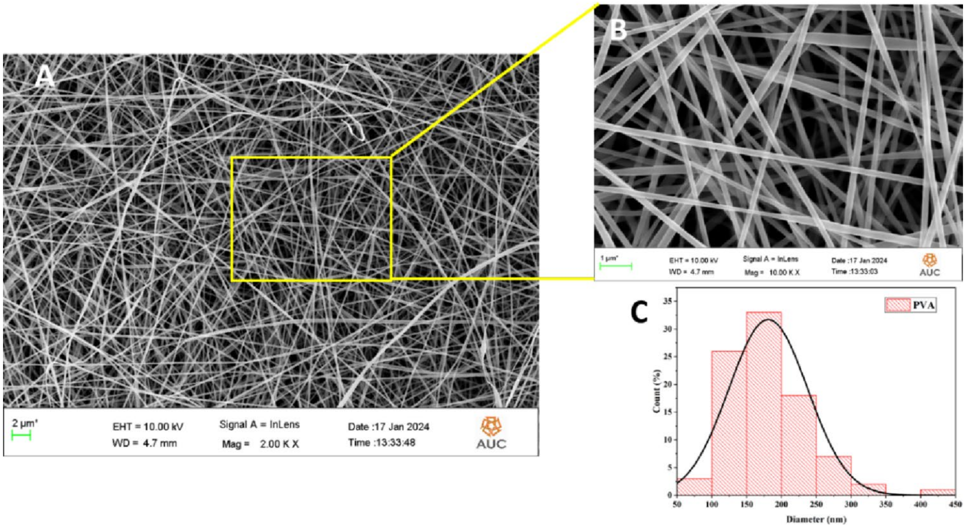

Fig. 8 FE-SEM analysis of the PVA 10% at Flow rate 0. 5 ml/hr., Voltage 20.9 mV (**A**) 2 µm magnification cross section (**B**) 1 µm magnification cross section (**C**) Histogram indicating the average diameter of the nanofiber

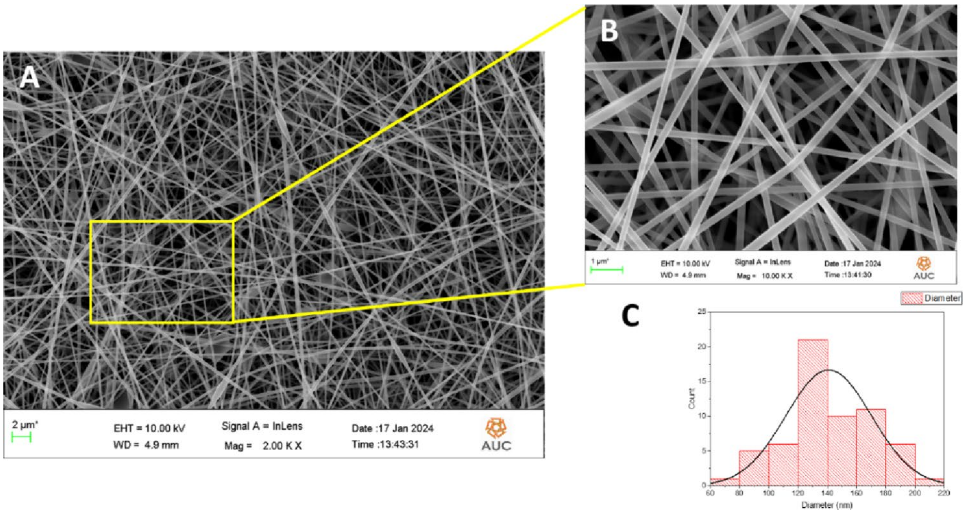

Fig. 9 FE-SEM analysis of the optimum PVA-UFBE nanofibers using parameters: algae concentration 2.48 mg/ml, Flow rate 0. 5 ml/hr., Voltage 20.9 mV, **A** 2 µm magnification cross section (**B**) 1 µm magnification cross section (**C**) Histogram indicating the average diameter of the nanofiber

OriginPro® 19 software analyses estimated the particle size to be approximately 16 nm. The SEM image of the PVA nanofiber (Fig. 8) demonstrated a uniform, bead-free fibrous morphology with an average fiber diameter of 168.5 nm. Upon incorporation of UFBE, the morphology of the composite nanofiber (Fig. 9) remained uniform with a slightly decreased average diameter of 133 nm. This reduction in fiber diameter suggests enhanced electrospinning ability due to the interaction between the hydroxyl groups of PVA and the sulfate and carboxyl groups present in the UFBE, as reported in FTIR analysis (Fig. 6), supporting the successful incorporation of the biopolymer within the fiber matrix. Regarding the cast film samples, the PVA film exhibited a smooth, homogenous surface (Fig. 10a), consistent with previously reported literature where PVA films prepared under controlled conditions demonstrated high structural uniformity (Le Van et al. 2019). In contrast, the SEM image of the PVA-UFBE film (Fig. 10b) showed dispersed UFBE particles distributed across the film surface. This observation further validates the integration of UFBE within the polymeric matrix and aligns with the FTIR findings, where new absorption bands and intensity changes indicated intermolecular interactions between the PVA chains and ulvan components. Additionally, cross-sections of the prepared films were examined using a Benchtop SEM (Neoscope JCM-6000 Plus, JEOL) to confirm the incorporation of UFBE particles into the film matrix. As shown in Fig. 10d, the UFBE components are diffused between the layers of the film, whereas the PVA film alone (Fig. 10c) exhibits a smooth surface. These results confirm the uniform dispersion of UFBE particles within the PVA film matrix.

To further confirm the integration of UFBE within the PVA film matrix, energy-dispersive X-ray (EDX) analysis was conducted using a Benchtop Scanning Electron Microscope (Neoscope JCM-6000 Plus, JEOL). The EDX analysis of UFBE, PVA nanofiber, PVA-UFBE nanofiber, PVA film, and PVA-UFBE film samples (Table 3 and Fig. 16S) display high atomic percentages of carbon (C), oxygen (O),

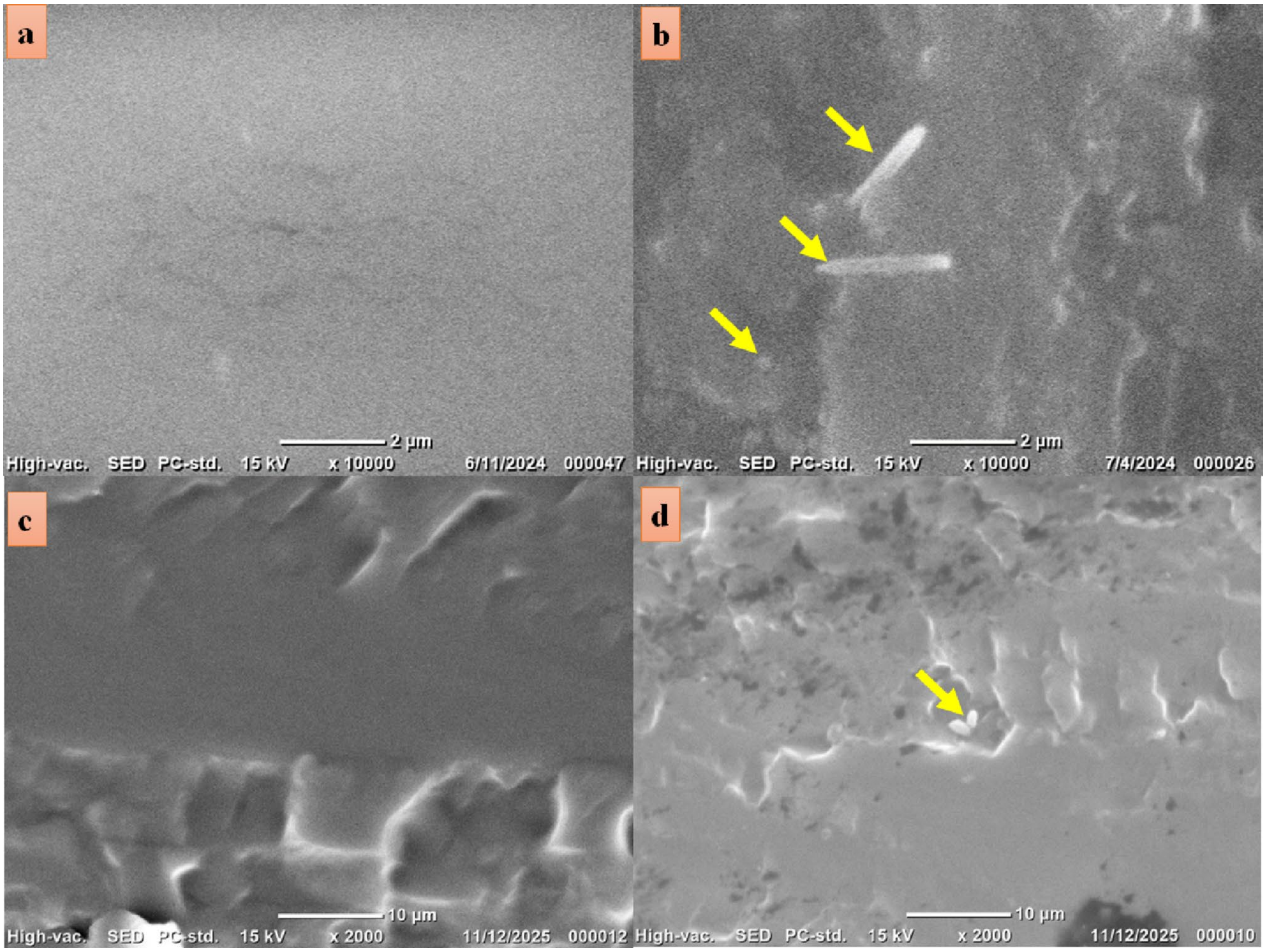

Fig. 10 BT-SEM analysis of the prepared (**a**) PVA 10%, 5 ml solvent casting evaporation (The film shows a smooth surface whereas the cracks are developed by the SEM beam), **b** PVA-UFBE films, **c** cross section of PVA film, and **d** cross section of PVA-UFBE film using parameters: algae concentration 2.48 mg/ml, PVA concentration 10%, 5 ml casting volume (Yellow arrows refers to the crystal structure of the embedded UFBE powder within the casting PVA film)

Table 3 EDX data of the prepared UFBE powder, PVA nanofiber, PVA-UFBE nanofiber, PVA film, PVA-UFBE film

Element	UBFE		PVA film		PVA-UBFE film		PVA nanofiber		PVA-UBFE nanofiber	
	Mass (%)	Atom (%)	Mass (%)	Atom (%)	Mass (%)	Atom (%)	Mass (%)	Atom (%)	Mass (%)	Atom (%)
C	7.36	14.84	83.55	87.12	80.48	84.96	84.24	87.69	83.04	87.05
O	14.8	22.39	16.45	12.88	18.41	14.59	15.76	12.31	15.87	12.49
Na	22.69	23.89	0	0	0.16	0.09	0	0	0.22	0.12
Mg	1.09	1.98	0	0	0.09	0.05	0	0	0.13	0.07
Si	0.35	0.3	0	0	0	0	0	0	0	0
S	9.55	7.21	0	0	0.38	0.15	0	0	0.22	0.09
Cl	41.31	28.21	0	0	0.32	0.11	0	0	0.48	0.17
Ca	1.95	1.18	0	0	0.16	0.05	0	0	0.04	0.01
Total	100	100	100	100	100	100	100	100	100	100

and sulfur (S), hallmark elements of algal extracts, together with notable levels of sodium (Na), magnesium (Mg), and chlorine (Cl). Upon embedding UFBE in PVA nanofibers or films, these distinctive elemental markers, particularly sulfur and chlorine, become evident in the PVA-UFBE composites but remain undetectable in the native PVA samples. For instance, sulfur is detected exclusively in the PVA-UFBE nanofibers (0.22 wt%, 0.09 at%) and PVA-UFBE films (0.38 wt%, 0.15 at%), while chlorine is also uniquely observed in the PVA-UFBE nanofibers (0.48 wt%, 0.17 at%) and PVA-UFBE films (0.32 wt%, 0.11 at%). The absence of these elements in pristine PVA confirms their origin from UFBE, validating the integration within the polymeric matrices and excluding the possibility of surface contamination. This finding is further substantiated by the observed decrease in the concentration of some elements within the composite samples relative to pure UFBE, indicating effective matrix dispersion rather than superficial adherence. These results are in strong agreement with existing literature, particularly the study by Nour Sh. El-Gendy et al., which demonstrated through EDX analysis that *Ulva fasciata*-derived materials contain elevated levels of carbon, oxygen, and sulfur, along with measurable amounts of sodium, magnesium, and chlorine. The elemental distribution reported in their work closely parallels the findings of the present study, establishing a reliable benchmark for EDX-based characterization of *Ulva fasciata* extracts incorporated into polymeric matrices (El-Gendy et al. 2023). Notably, the presence of distinct sulfur peaks further supports the identification of sulfated ulvan groups, which are a hallmark of seaweed-derived polysaccharides in composite systems. Thus, the EDX spectra obtained in this study verify effective UFBE immobilization within PVA nanofibers and films. Additionally, the elemental profiles observed here align with recognized standards for *Ulva fasciata* extracts, thereby directly linking these findings to established benchmarks in seaweed-based biomaterial characterization.

Thermogravimetric analysis (TGA) and derivative thermogravimetry (DTG) analysis

The prepared PVA nanofiber, PVA-UFBE nanofiber, PVA film, and PVA-UFBE film membranes were characterized using TGA analysis before and after heat treatment. Additionally, the UFBE was analyzed using TGA and DTG that were plotted and presented in Fig. 11. Figure 11a shows the TGA and DTG analysis of the UFBE powder. A mass loss of nearly 38% was observed at 400 °C, 11.2% at 500 °C, and 3.6% at 600 °C that could be attributed to the organic matter decomposition and the carbonization of the Ulvan organic and non-volatile constituent's carbonization. Whereas the DTG analysis showed nearly three main decomposition peaks at nearly 300, 350, 420 °C. This result is nearly the results obtained by Ulvan recorded in the previous work of El-Gendy et al. (El-Gendy et al. 2023). The PVA nanofiber Fig. 11b showed a mass loss of around 6% in the region of 0–100 °C followed by a loss of 18.1% between 100 and 200, and the final mass loss was 9.5% at 400–700 °C. While the DTG analysis showed three characteristic peaks at 100, 200, and 700 °C. By combining the UFBE with PVA to form PVA-UFBE nanofiber Fig. 11C with a mass loss of nearly 35% at a temperature of 300–400 °C, then 12% at 400–500 °C, and 4% at a temperature range of 500–650 °C. The three decomposition peaks of DTG analysis are 390, 400, and 450 °C. Figure 11D shows the TGA and DTG analysis of the PVA-UFBE nanofiber after the heat treatment which showed the main decomposition peaks of the DTG analysis at two main peaks 300 and 400 °C. The TGA analysis shows a loss in mass up to 350 °C with a percentage of 40.8%, and a mass loss of 7.99% in the range of 350 to 500 °C. Nevertheless, the TGA analysis of PVA-UFBE films in comparison to the PVA films are represented in Fig. 11e and f, a percent of approximately 12.5% of weight loss was observed for the PVA film before heating Fig. 11e at temperatures between 100 and 200 °C that is decreased to 6.5% by adding the UFBE powder in the PVA-UFBE film Fig. 11f. Afterward, a decomposition was noticed in the temperature region from 200 to 400 to be around 68% for the PVA film, whereas 64% for the PVA-UFBE film. The final weight loss was stated at the region of 400 to 500 °C to be 17, and 23 for the PVA and PVA-UFBE film, respectively. The three main decomposition points for the PVA film and PVA-UFBE film were 100 & 300 & 400 °C and 100, 400, and 450 °C for the PVA film, and the PVA-UFBE film. Whereas, after heat treatment of the PVA-UFBE film Fig. 11g, it was noticed that weight loss at a temperature range of 100–200 °C decreased to 2.3%, unlike 6.5% before the PVA-UFBE film heat treated. After that, the second weight loss was shifted to a temperature between 300 and 400 °C to be nearly around 76% and the final weight loss gets to less than one at temperature range of 500–600 °C. Whereas the DTG analysis of the PVA-UFBE film showed two decomposition peaks at nearly 350 and 450 °C. These thermal results strongly support the successful integration of UFBE into both nanofiber and film matrices. The shift in decomposition temperatures and reduced early-stage weight loss after UFBE incorporation and heat treatment indicate improved thermal stability and intermolecular interactions.

X ray diffraction (XRD)

The X-ray diffraction (XRD) patterns of UFBE powder, PVA nanofiber, PVA-UFBE nanofiber, PVA film, and PVA-UFBE film are presented in Fig. 12. UFBE powder exhibited distinct peaks at approximately 9.8°, 19.5°, 28.7°, 38.5°, and 49.3° (2θ), reflecting a pronounced crystalline nature consistent with UFBE powder as previously characterized by (El-Gendy et al. 2023). These sharp reflections correlate with the presence of carbohydrate-based biopolymers and various bioactive compounds recovered in macroalgal extracts, as validated by integrated biorefinery processes for *Ulva fasciata*. Pure PVA nanofibers and films revealed a broad peak around 19.5° (2θ), confirming their semi-crystalline morphology, in line with established literature for PVA materials (Alwan et al. 2016). Upon incorporation of UFBE into the PVA matrix, both nanofiber and film samples

Fig. 11 TGA and DTG analysis of the **a** UFBE powder, **b** PVA nanofiber, **c** PVA-UFBE nanofibers, **d** PVA-UFBE nanofibers/heat treated, **e** PVA film, **f** PVA-UFBE film **g** PVA-UFBE film/heat treated

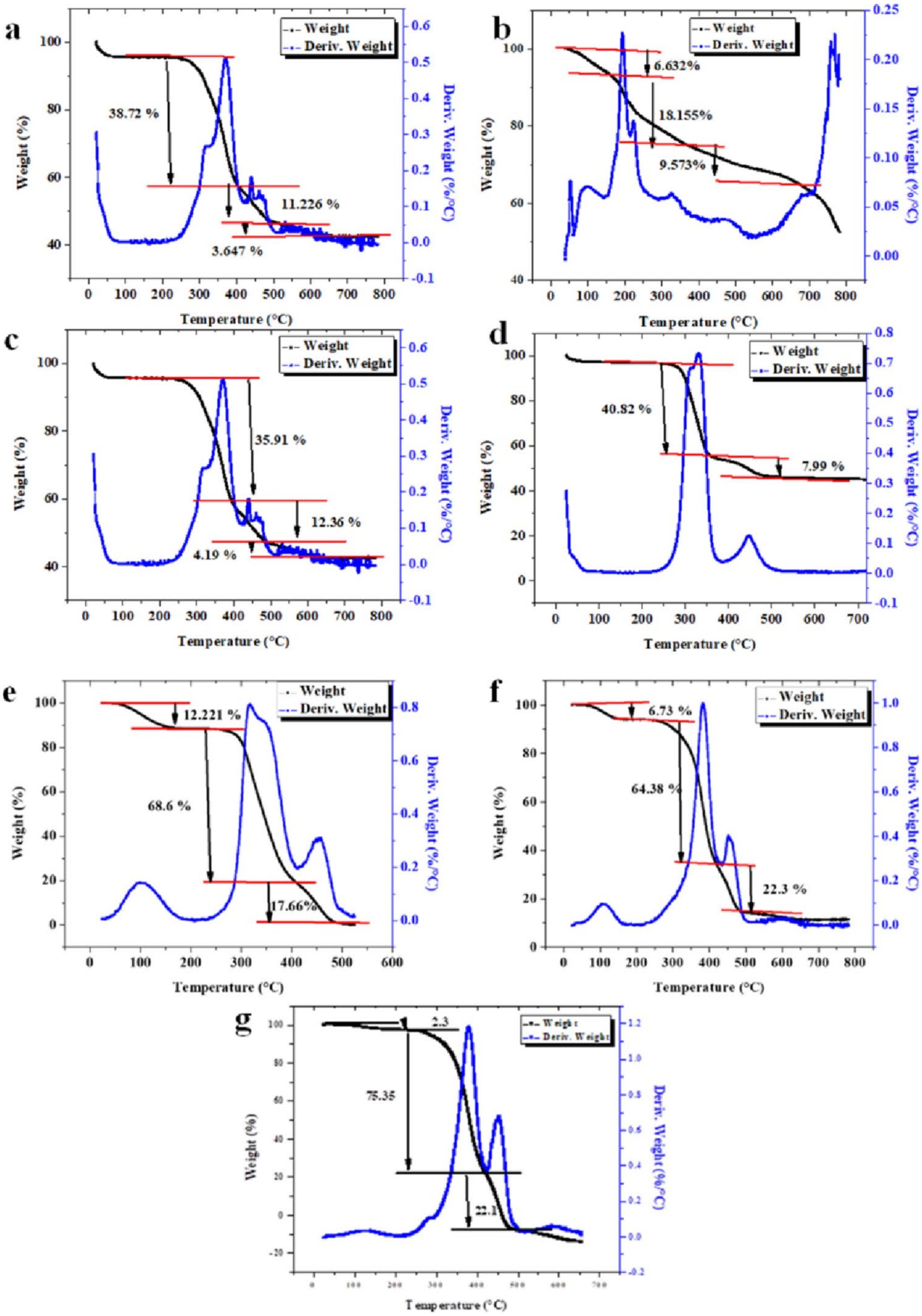

displayed clear spectral changes: the PVA-UFBE nanofiber exhibited increased peak intensity at 19.5° and additional minor peaks attributed to UFBE, signifying successful immobilization within the nanofiber structure. Similarly, PVA-UFBE films showed a combination of PVA's broad diffraction feature and subtle UFBE-related peaks, indicating efficient dispersion of UFBE in the film matrix. These findings align with previous research where the encapsulation of bioactive plant extracts within polymeric systems modulated composite crystallinity and improved their functional properties (Siddaiah et al. 2018). Overall, the XRD results strongly confirm the effective immobilization and homogeneous dispersal of UFBE in both PVA nanofibers and films, as evidenced by the coexistence and modification of respective characteristic diffraction signals, in agreement with both macroalgal extract and polymer literature.

Fig. 12 XRD analysis of the different samples prepared

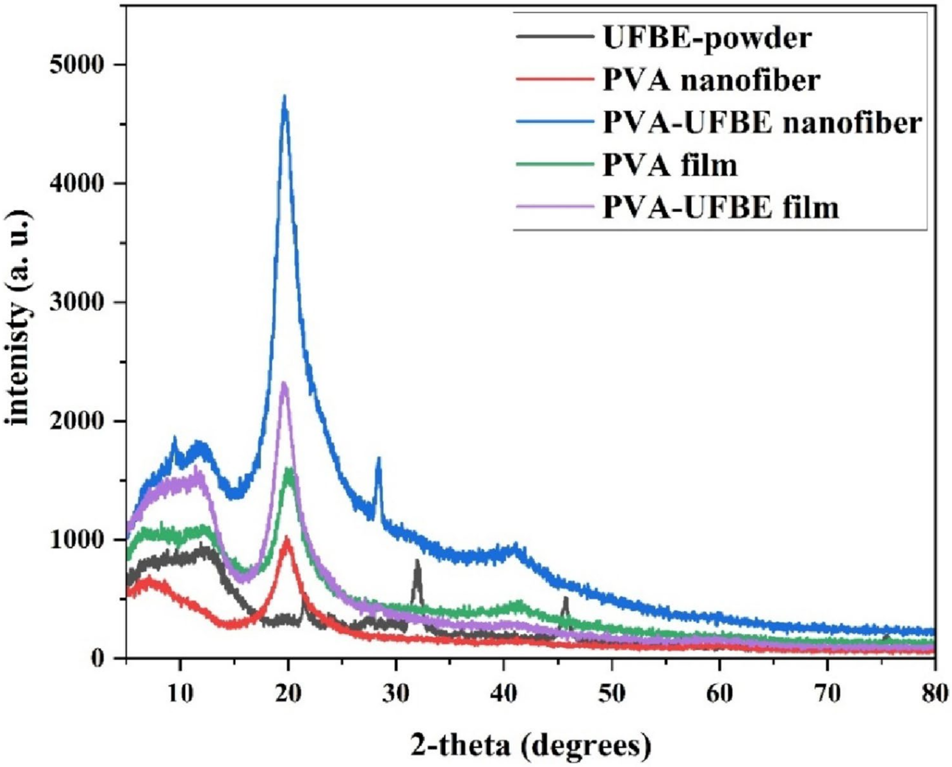

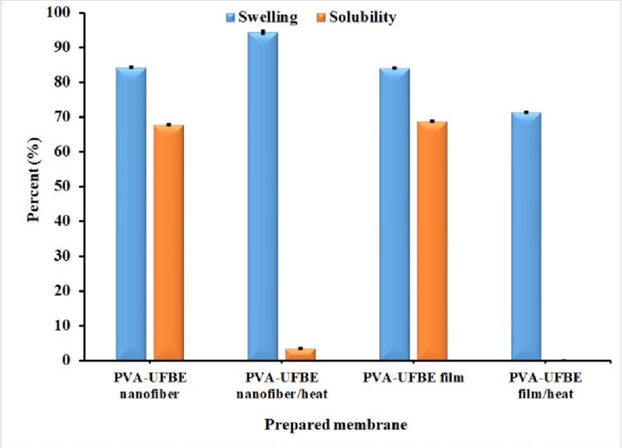

Fig. 13 Swelling and solubility properties of PVA-UFBE nanofiber and films before and after the heat treatment

Swelling and solubility results

Water solubility and swelling tests were conducted to evaluate the structural integrity and water degradability of the fabricated membranes. Additionally, it aims to assess the influence of heat treatment on their performance under prolonged aqueous exposure. Figure 13 presents the solubility and swelling behavior of the various membrane types after immersion in water for 48 h. The solubility test revealed that untreated PVA nanofibers underwent complete physical degradation, forming a gel-like structure that was unmanageable and unable to retain its original morphology. This outcome reflects the inherent hydrophilicity and water-soluble nature of polyvinyl alcohol, which limits its direct use in aqueous filtration applications without further stabilization. In contrast, the incorporation of the UFBE into the PVA matrix significantly improved water resistance. The solubility of the PVA-UFBE nanofiber and film membranes was reduced to approximately 70%, suggesting enhanced intermolecular interactions between the bioactive ulvan content in UFBE and the PVA chains. These interactions likely include hydrogen bonding and partial crosslinking, as also supported by FTIR analysis (Fig. 6), which showed characteristic shifts in hydroxyl and ether stretching regions indicative of new bonding interactions. Crucially, heat treatment of the PVA-UFBE membranes further reduced solubility to approximately 5% for nanofibers and effectively 0% for films, with both retaining their structural integrity and handling stability post-immersion. These findings highlight the efficacy of thermal post-treatment in enhancing water stability, most likely by promoting physical crosslinking and partial crystallization of the PVA matrix. The resulting increase in thermal and structural stability is consistent with TGA analysis (Fig. 11), which showed improved thermal decomposition profiles following heat treatment. In contrast, swelling behavior remained relatively constant across all membrane samples, suggesting that while heat treatment effectively reduced solubility, it did not significantly alter the membranes' capacity to absorb water. This may be advantageous in filtration applications where permeability must be maintained despite structural reinforcement. These results are consistent with previous studies that have demonstrated the importance of thermal treatment in stabilizing PVA-based membranes for aqueous applications. For example, it was reported that heat treatment induces chain entanglement and crystallization in PVA matrices, reducing solubility without compromising porosity (Es-Saheb and Elzatahry 2014; Enayati et al. 2016; Aktürk et al. 2019). Overall, the combined effects of UFBE incorporation and heat treatment provided a synergistic improvement in membrane stability, supporting their practical use in wastewater treatment processes, particularly under continuous or prolonged exposure to aqueous environments. These findings are in line with the membrane's performance in real wastewater conditions, where both nanofiber and film formats exhibited high removal efficiency without physical degradation, thus validating the structural improvements achieved through material and process optimization.

Determination of pore size; Brunauer–Emmett–Teller (BET) analysis

The porous characteristics of the fabricated membranes were evaluated using Brunauer–Emmett–Teller (BET) analysis, and the results are summarized in Table S3 and Fig. 14. The BET pore size analysis revealed that the PVA-UFBE nanofibers exhibited the highest average pore diameter (8.31 nm), followed by PVA nanofibers (7.51 nm), PVA-UFBE film (6.24 nm), and PVA film (1.87 nm). In terms of specific surface area, the nanofiber-based membranes also outperformed their film counterparts, with values of 12.94 m²/g and 11.15 m²/g for PVA-UFBE and PVA nanofibers, respectively, compared to 3.23 m²/g and 2.34 m²/g for the PVA-UFBE and PVA films. These results confirm that electrospun nanofibers provide significantly higher surface area and porosity than solvent-cast films, due to their inherently porous network and fiber-level architecture. The incorporation of UFBE further increased the surface area and pore size, likely due to the molecular interaction between the hydrophilic ulvan and the PVA matrix, which creates more open fiber packing and interconnected voids

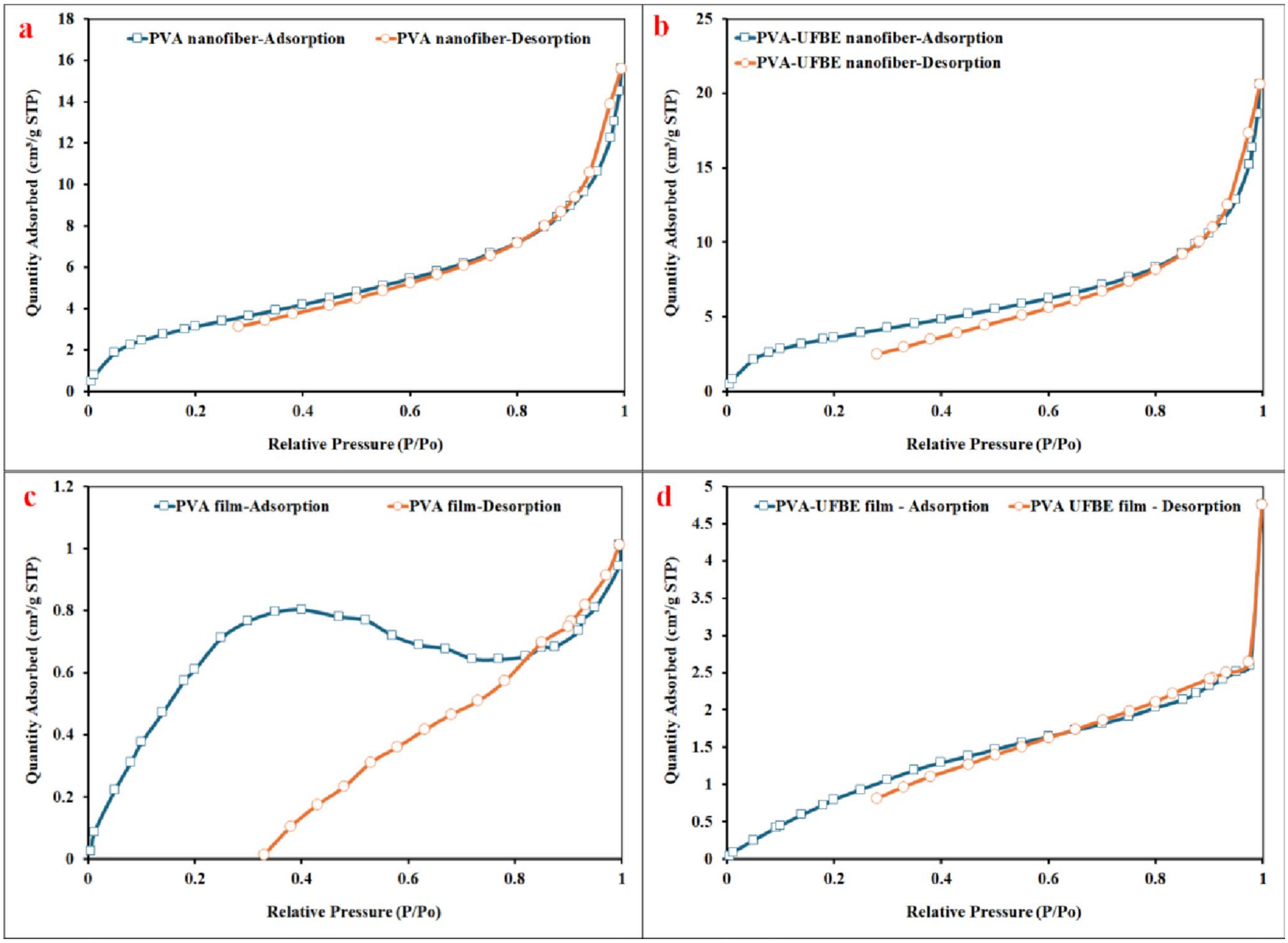

Fig. 14 Isothermal linear plot of **a** PVA nanofiber, **b** PVA-UFBE nanofiber, **c** PVA film, and **d** PVA-UFBE film

(Agüero et al. 2023). Similar pore size ranges for electrospun membranes (6–8 nm) have been previously reported in the literature for comparable polymer-based filtration materials (Taha et al. 2024). The enhanced porosity and surface area of the PVA-UFBE nanofiber membrane are in strong agreement with its superior swelling capacity (Sect. X Ray Diffraction (XRD)) and higher contaminant accumulation observed in post-filtration SEM analysis (Fig. 11. These structural advantages facilitated greater water permeability and increased interaction with suspended particulates, thus reinforcing the membrane's effectiveness for wastewater treatment.

Tensile strength

The mechanical strength of the fabricated membranes was evaluated using uniaxial tensile testing, and the corresponding stress-strain curves are presented in Fig. 15. The tensile strength measurements revealed distinct differences among the membrane formats. The PVA nanofiber and PVA-UFBE nanofiber membranes exhibited tensile strengths of 9.79 MPa and 4.41 MPa, respectively, while the PVA film and PVA-UFBE film demonstrated significantly higher strengths of 30.09 MPa and 46.80 MPa. These values are consistent with literature-reported tensile strengths for PVA-based films, which typically range from 25 to 35 MPa depending on polymer concentration and processing conditions (Liu et al. 2013). The relatively low tensile strength observed in both nanofiber membranes can be attributed to the inherently porous and discontinuous fibrous architecture produced by electrospinning, which limits effective stress transfer between fibers and reduces overall mechanical integrity. In contrast to dense films, electrospun nanofiber mats exhibit weak inter-fiber bonding and limited chain entanglement, making them more susceptible to mechanical deterioration upon elongation (Huang et al. 2003; Ramakrishna 2005). The further reduction in tensile strength observed in the PVA-UFBE nanofiber membrane is attributed to the plasticizing effect of the hydrophilic UFBE within the nanofibrous network. The presence of UFBE disrupts intermolecular PVA-PVA interactions and reduces fiber stiffness and inter-fiber cohesion, particularly in the highly surface-exposed nanofiber system, where moisture uptake and molecular mobility are amplified (Greiner and Wendorff 2007). Despite their lower mechanical strength, nanofiber membranes offer enhanced flexibility and surface area, factors advantageous for filtration performance and surface adsorption. In contrast, the cast film membranes showed markedly superior mechanical stability, with the PVA-UFBE film outperforming all other membranes. In film systems, the dense and continuous morphology allows UFBE to act as a reinforcing biopolymeric phase. The extended drying time and compact polymer packing facilitate stronger intermolecular hydrogen bonding between

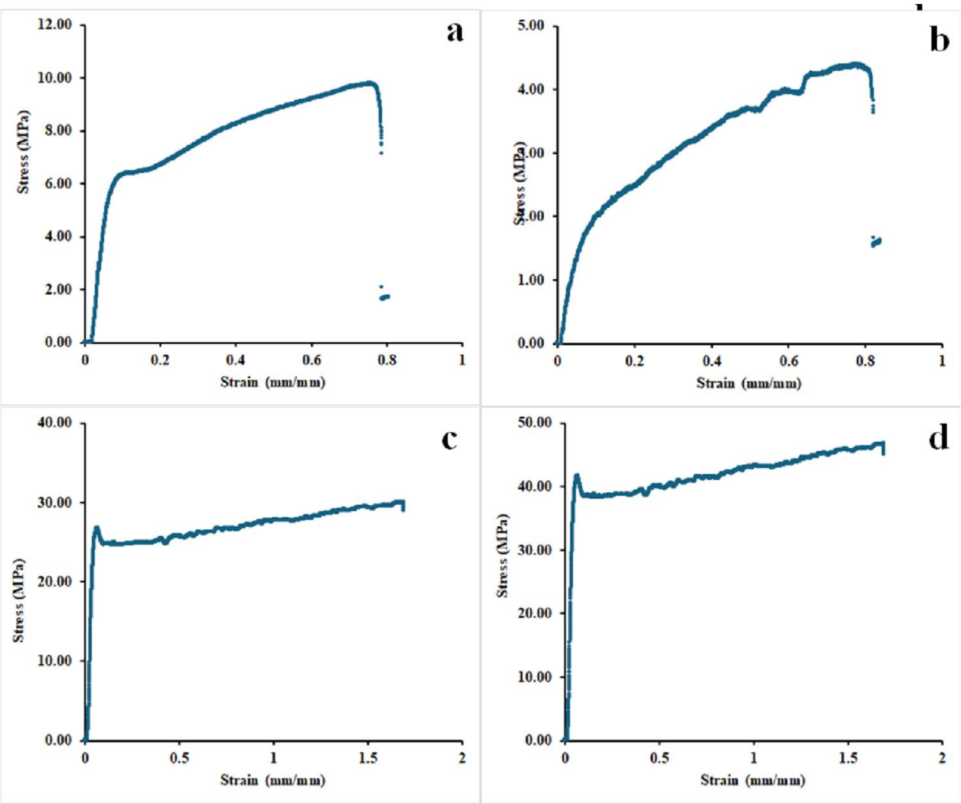

Fig. 15 Tensile stress plotting of **a** PVA nanofiber, **b** PVA-UFBE nanofiber, **c** PVA film, and **d** PVA-UFBE film

PVA hydroxyl groups and UFBE functional groups, resulting in improved stress distribution and load-bearing capacity (Silva et al. 2013; Zhang et al. 2025). This enhancement suggests a reinforcing effect of the biopolymer, contributing to a more cohesive and mechanically robust matrix. These mechanical advantages correlated strongly with the filtration performance, particularly in terms of scale-reducing ion capture. The higher tensile strength and lower swelling ratio of the PVA-UFBE film supported its ability to withstand ionic loading during filtration and resist surface deformation, leading to higher removal of hardness, alkalinity, and scale-forming ions (as described in Sect. Complete water analysis results). Collectively, these findings illustrate a functional trade-off between membrane formats: nanofibers provide elevated porosity and reactive surface area conducive to the removal of dispersed and hydrophobic pollutants (e.g., oil and turbidity), whereas films offer mechanical resilience and structural stability essential for efficient ionic pollutant filtration and sustained operational durability. Notably, the contrasting mechanical response of UFBE in nanofibers and films highlights the critical role of membrane morphology and processing route in governing the functional behavior of hydrophilic biopolymer additives. This correlation between mechanical properties and pollutant selectivity emphasizes the critical importance of tailoring membrane architecture to effectively target specific contaminants.

Complete water analysis results

To assess the filtration performance of the developed membranes, four types, PVA nanofiber, PVA-UFBE nanofiber, PVA film, and PVA-UFBE film, were applied to real formation water obtained from the outlet of an API separator in an oilfield. A commercial filter paper was included for comparison. The wastewater sample, aged for three months to reflect post-degradation, low-concentration pollutant conditions, provided a challenging model relevant to tertiary treatment or polishing applications. Full physicochemical analysis was conducted before and after membrane treatment (Table 4), and removal efficiencies are summarized in Table S4. Among the tested membranes, the PVA-UFBE nanofiber, PVA nanofiber, and PVA-UFBE film all achieved complete removal of oil (from ~12.5 mg/L to 0 mg/L), far outperforming the commercial filter, as represented in Fig. 16. This can be attributed to the presence of dissolved organic pollutants, which serve as additional hydrophobic active sites on the surface of the membrane. These sites then function as new sorption sites, as described by Liu, et al. (Liu et al. 2020; Nassar et al. 2022). In addition, the existence of salts in seawater would decrease the electrostatic repulsion between the oil and the surface of the membrane, thus increasing the ability of the membrane oil sorption (Boleydei et al. 2018). The PVA-UFBE nanofiber also demonstrated the highest turbidity removal efficiency (Fig. 17), reducing turbidity from ~19 NTU to ~3 NTU (82.9% reduction). This performance is consistent with the membrane's high surface area, enhanced porosity, and uniform nanoscale fiber morphology observed in the BET and SEM analyses (Sect. Scanning electron microscope analysis and Swelling and solubility results). In contrast, the PVA-UFBE film exhibited superior performance in reducing ionic content, including total hardness (from ~16,768 to 14,972 mg/L as $CaCO_3$) and alkalinity (from ~209 to 77 mg/L), See Fig. 18. This trend reflects the film's greater tensile strength (46.8 MPa), lower swelling ratio, and thermal stability, as shown in TGA and tensile strength data (Sect. Thermogravimetric analysis (TGA) and Derivative thermogravimetry (DTG) analysis and Determination of pore size; Brunauer–Emmett–Teller (BET) analysis). The effective retention of ionic species is attributed to the functional groups introduced by UFBE, such as carboxylates and sulfates, which promote ionic binding and scale-forming ion capture. Notably, bicarbonate, calcium, and strontium, all major contributors to scaling, were significantly reduced after filtration, particularly by the PVA-UFBE film. These changes directly contributed to a 76.6% reduction in calculated scale formation tendency (Table 5), as modeled using OLI ScaleChem under representative operational conditions. The membranes also contributed to improvements in other critical parameters. For instance, iron concentrations were reduced by nearly 80% using the PVA-UFBE nanofiber, while calcium and carbonate were reduced by 10.6% and 63.3%, respectively, with the PVA-UFBE film. The tabulated effective elimination of ammonium (Fig. 19a) was also significant, helping reduce eutrophication potential, a known ecological risk associated with nitrogen species in wastewater (Barbieri and Bondioli 2015; Salbitani and Carfagna 2021). Whereas, the decrease in alkalinity (Table 4 and Fig. 18) is related to the concomitant removal of bicarbonate (Table 4 and Fig. 19b), and it is considered beneficial for the decrease in scale tendency (Nassar et al. 2022). Moreover, the noted reductions in strontium and iron (Table 4) support corrosion and scaling resistance, important for long-term system maintenance (Sen et al. 2011). Despite the low contaminant concentrations present in the aged wastewater sample, the PVA-UFBE membranes exhibited remarkable sensitivity and selectivity. This performance underscores their potential application in polishing or tertiary treatment stages where selective removal of residual contaminants is critical, and conventional membranes often fall short. These results are strongly supported by the structure-function relationships established through comprehensive characterization. Specifically, the PVA-UFBE nanofibers exhibited a markedly higher specific surface area (9.93 m²/g), and total

Table 4 Complete water analysis of the wastewater sample before and after treatment by various membranes

Parameter	Raw water	Filter paper	PVA-nanofiber	PVA-UFBE nanofiber	PVA film	PVA-UFBE film
Total Dissolved Solids (T.D.S.) mg/L	67372.68	59614.50	56499.01	56773.19	59405.36	55608.45
Salinity (as NaCl) mg/L	61664.14	53974.31	52570.11	52103.70	55343.64	51757.20
Alkalinity (as $CaCO_3$) mg/L	208.60	111.30	86.80	95.50	105	76.50
Total Hardness (as $CaCO_3$) mg/L	16768.23	16287.16	15019.09	16034.92	16407.14	14972.39
Oil Content mg/L	12.50	2.10	0	0	1.25	0
Turbidity NTU	19.40	5.22	3.59	3.31	4.72	3.63
Density @ 60 F g/ml	1.04	1.02623	1.04	1.04	1.04	1.03
Specific gravity	1.45	1.02725	1.04	1.04	1.04	1.03
pH @ 25 °C	7.44	7.48	7.47	7.52	7.49	7.65
Conductivity µS/cm @25 °C	84,200	84,000	85,100	84,700	85,500	84,300
Resistivity Ohm-m @25 °C	0.12	0.119	0.12	0.12	0.117	0.12
Lithium mg/L	0.67	Nil	Nil	Nil	Nil	Nil
Sodium mg/L	19908.51	16372.93	15566.50	15726.60	16190.50	15,267
Ammonium mg/L	14.59	4.7	1.06	2.12	13.90	4.43
Potassium mg/L	448.03	440.17	326.29	348.96	433	339.18
Magnesium mg/L	1258.23	1201.62	1129.40	1152.80	1208.25	1119.23
Calcium mg/L	4640.30	4541	4152.27	4520.50	4578.12	4150.34
Strontium mg/L	26.80	Nil	Nil	Nil	Nil	Nil
Barium mg/L	Nil	Nil	Nil	Nil	Nil	Nil
Iron mg/L	3.11	0.54	0.46	0.61	0.48	0.5
Cupper mg/L	Nil	Nil	Nil	Nil	Nil	Nil
Fluoride mg/L	Nil	Nil	Nil	Nil	Nil	Nil
Chloride mg/L	37372.20	32711.70	31860.67	31,578	33541.60	31,368
Bromide mg/L	1008.44	981.34	934.70	881.84	883.60	841.70
Nitrate mg/L	787.20	782	781	780.70	782.35	775.76
Nitrite mg/L	Nil	Nil	Nil	Nil	Nil	Nil
Phosphate mg/L	Nil	Nil	Nil	Nil	Nil	Nil
Sulfate mg/L	1679.40	1669.22	1640.79	1664.70	1645.40	1649
Hydroxide mg/L	Nil	Nil	Nil	Nil	Nil	Nil
Carbonate mg/L	Nil	Nil	Nil	Nil	Nil	Nil
Bicarbonate mg/L	254.37	135.73	105.84	116.51	128.10	93.33

pore volume (0.0415 cm^3/g) compared to their film counterparts, along with a larger average pore size of approximately 15.38 nm. These features contributed to a more open and porous nanostructure, enabling increased water permeability and enhanced exposure of active adsorption sites during filtration. As a result, post-filtration SEM images (Fig. 20) revealed a more pronounced accumulation of particulate matter on the surface of the nanofiber membranes relative to the films, indicating more effective physical entrapment and interaction with residual wastewater contaminants. This behavior is further corroborated by swelling analysis, where the nanofibers demonstrated higher swelling ratios prior to heat treatment, consistent with their elevated hydrophilicity and water uptake capacity. Such characteristics are advantageous for the removal of suspended solids and dispersed hydrophobic pollutants like oil and turbidity. In contrast, the PVA and PVA-UFBE films, characterized by smoother, less porous surfaces and higher mechanical strength, exhibited lower swelling and significantly reduced fouling, evidenced by minimal surface deformation after use. These attributes explain their superior performance in retaining hardness-causing ions and minimizing scale formation. Collectively, these findings establish a coherent relationship between microstructural properties and functional performance. The integration of UFBE into the nanofiber matrix enhanced both morphological uniformity and porosity, translating into improved adsorption-driven pollutant removal. Meanwhile, in the film format, UFBE incorporation improved mechanical durability and ionic selectivity without compromising structural integrity. This structure-function synergy substantiates the membranes' complementary roles in real wastewater treatment and supports their tailored application in advanced, selective, and scalable filtration systems. Overall, the PVA-UFBE nanofiber is most effective for oil and turbidity reduction, whereas the PVA-UFBE film is more efficient for scaling ion removal and hardness control. These results confirm that membrane structure and format can be tailored to specific wastewater treatment needs. Moreover, the ability of these membranes to perform effectively under

Fig. 16 Oil content of water sample before and after treatment by various membranes

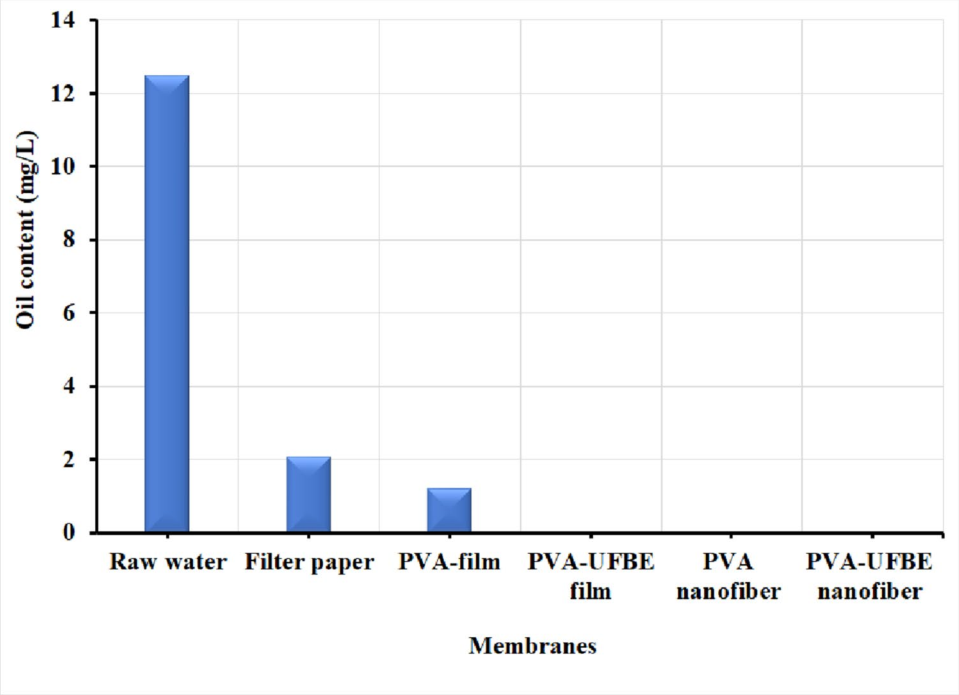

Fig. 17 Turbidity of water sample before and after treatment by various membranes

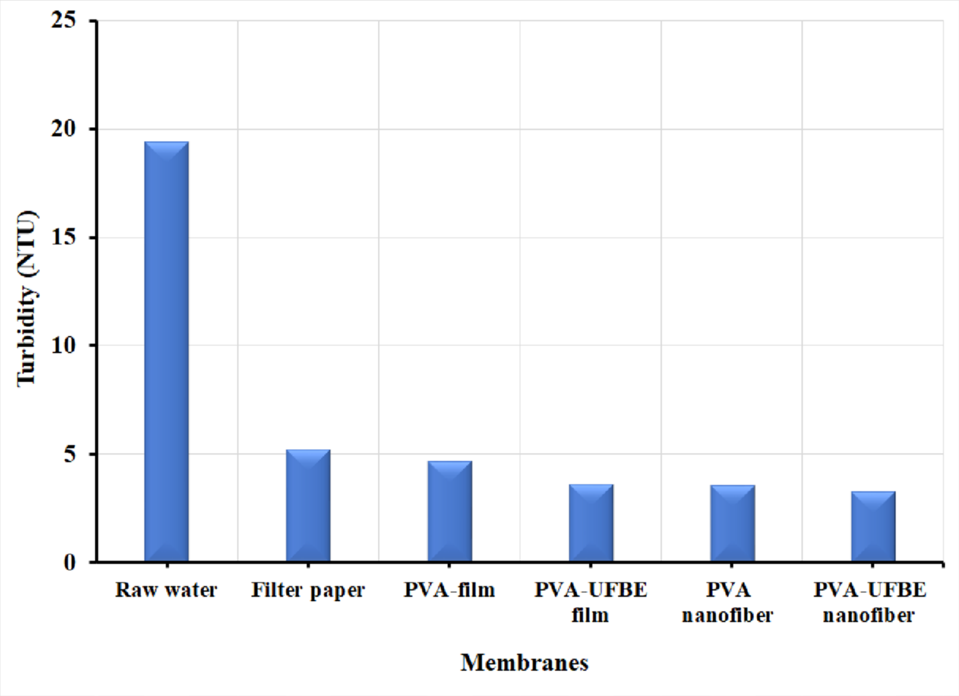

low-contaminant conditions highlights their potential for application in advanced or tertiary treatment stages.

To further substantiate the filtration performance of the developed membranes, SEM imaging was conducted before and after exposure to wastewater, providing direct evidence of structural changes associated with contaminant capture (Fig. 20). The pristine nanofiber membranes (Fig. 11a, c) exhibited a highly porous, interconnected network with uniform fiber distribution, whereas the films displayed relatively smooth and compact surfaces (Fig. 20e, g). Following wastewater treatment, pronounced surface fouling became apparent, particularly on the nanofiber membranes, where substantial particulate accumulation and localized structural deformation were observed (Fig. 20d, e). These morphological alterations confirm the strong physical entrapment of suspended solids, oil droplets, and fine particulate matter

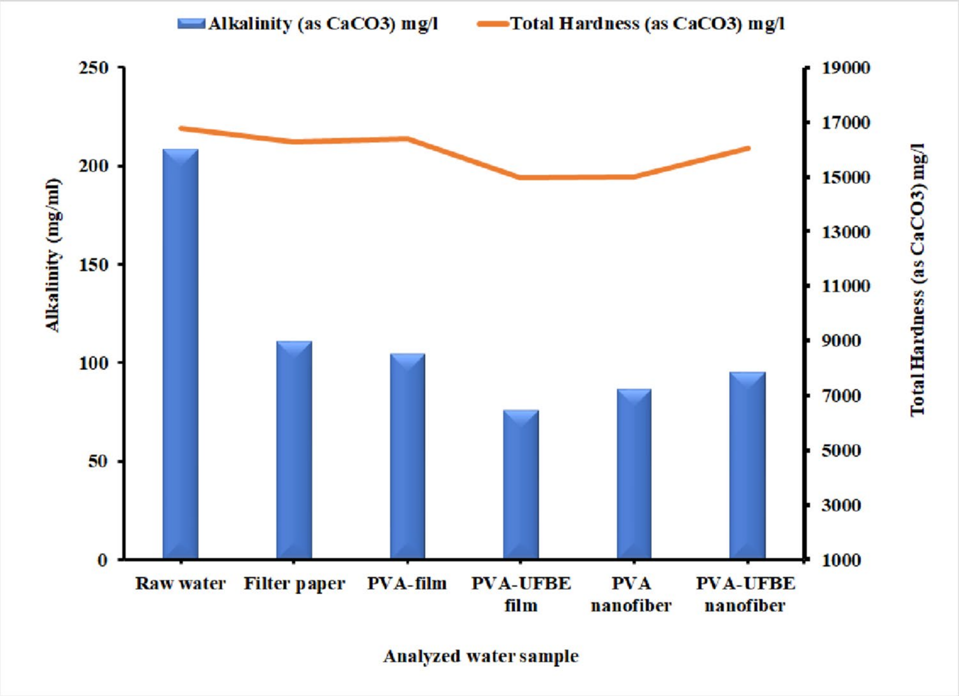

Fig. 18 Total hardness and alkalinity as $CaCO_3$ of water sample before and after treatment by various membranes

Table 5 Scale and corrosion tendency by various membranes

Sample	Scale mineral	Maximum scale		Decrease possibility of scale formation %	Aggressiveness (AI)*		Alkalinity**		Puckorius scaling index (PSI)***	
		mg/L	lb/bbl		Value	Type	mg/L	Type	Value	Type
Raw water	$CaCO_3$	56.0	0.0196	---	13.8	Non	208.6	V. high	3.62	Tendency to lime scale
Filter paper	$CaCO_3$	15.3	0.0053	72.68	13.6	Non	111.3	High	4.58	Optimum range
PVA-film	$CaCO_3$	14.0	0.0049	75.00	14.7	Non	105	High	4.66	Optimum range
PVA-UFBE film	$CaCO_3$	13.1	0.0046	76.61	13.4	Non	76.5	Medium	5.23	Optimum range
PVA nanofiber	$CaCO_3$	13.6	0.0047	75.71	13.4	Non	86.8	Medium	5.04	Optimum range
PVA-UFBE nanofiber	$CaCO_3$	17.5	0.0061	68.75	13.6	Non	95.5	Medium	4.82	Optimum range

*AI > 12: Water has scaling property (non-aggressive & non-corrosive) 10 < AI < 12: Water is approximately corrosive AI < 10: Water is severely corrosive (very aggressive)

**Alkalinity > 20: not corrosive 41–98.4: Medium 98.4–147.6: High > 147.6: Very high

***PSI < 4.5: Tendency to lime scale 4.5 < PSI < 6.5: Optimal range PSI < 6.1: Scaling is unlikely to occur PSI > 6.5: Water tends to corrosion

within the nanofibrous architecture, supporting the high turbidity and oil removal efficiencies recorded for these membranes. In contrast, the post-filtration images of the films (Fig. 20f, h) exhibited only minimal surface deposits and negligible distortion, consistent with their lower swelling ratio, higher mechanical stability, and selective interaction with dissolved ionic species rather than particulate pollutants. These SEM findings align with the overall microstructural characteristics, high surface area, larger pore volume, and enhanced hydrophilicity in nanofibers versus dense, mechanically robust film matrices, thereby reinforcing the structure, function relationships discussed in the results section. Collectively, the before-and-after SEM analyses validate that the nanofiber membranes are particularly effective for particulate-based removal mechanisms (oil, turbidity, residual organics), whereas the PVA-UFBE films primarily facilitate ionic retention with minimal fouling. This integrated morphological evidence complements the physicochemical performance data and supports the applicability of these membranes for differentiated roles in advanced and tertiary wastewater treatment.

Conclusion

The present study demonstrates the effective development of environmentally friendly composite membranes for advanced wastewater treatment through the integration of

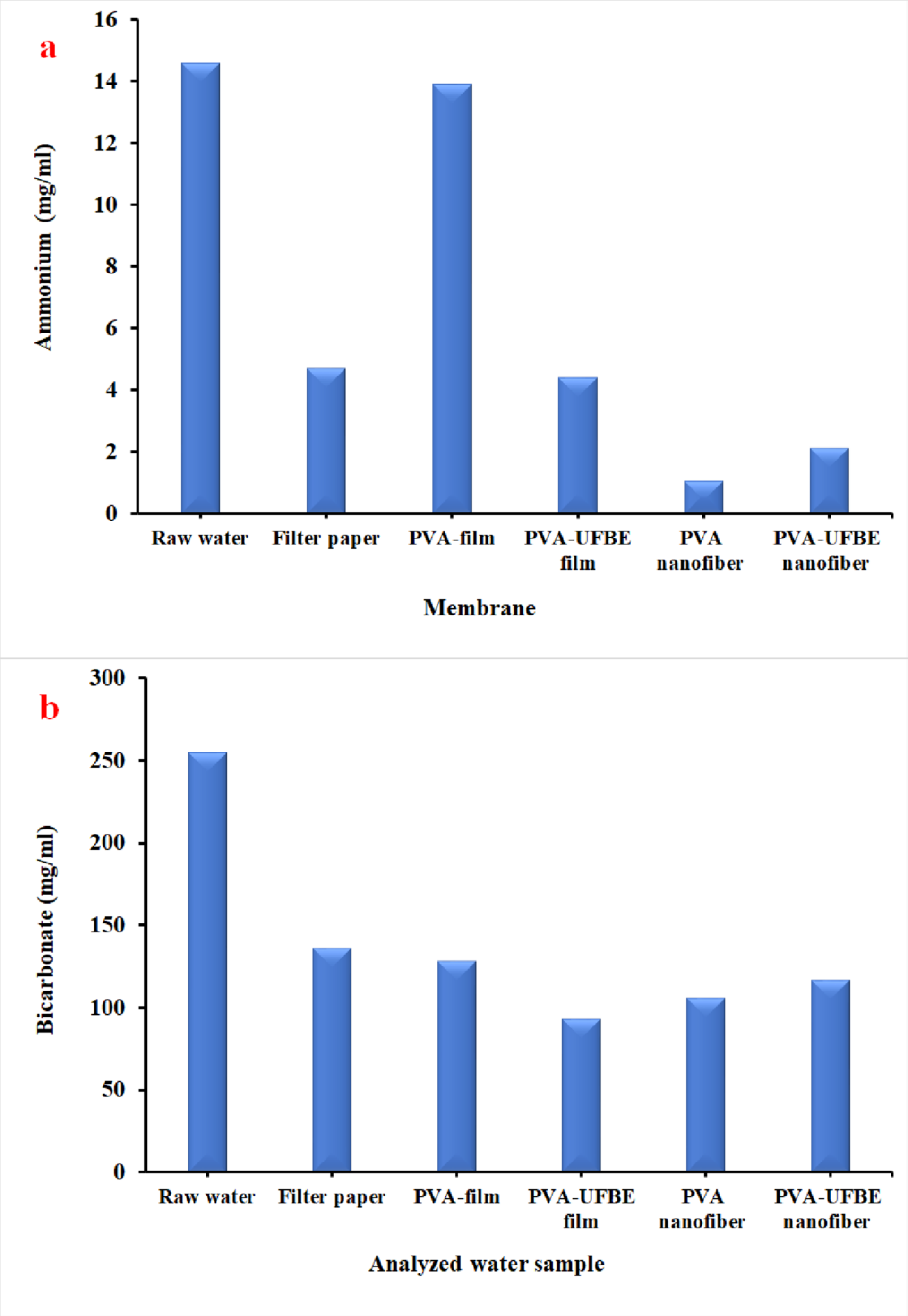

Fig. 19 **a** Ammonium, and **b** bicarbonate of water sample before and after treatment by various membranes

bioactive compounds from *Ulva fasciata* bioethanol byproduct extract (UFBE) into a polyvinyl alcohol (PVA) matrix. The fabricated PVA-UFBE membranes, prepared in nanofiber and film configurations, exhibited tunable porosity, enhanced mechanical robustness, low water solubility, and promising anti-biofouling potential attributed to the ulvan content, as verified by FTIR and SEM analyses. Optimization via Box–Behnken response surface methodology identified ideal fabrication conditions at 10% PVA, 2.49 mg/mL UFBE, a flow rate of 0.5 mL/h, 20.9 kV applied voltage, and a 16 cm collector distance. Post-fabrication thermal treatment further strengthened the membranes, reducing solubility from nearly 70% to below 5%, thus ensuring structural stability in aqueous environments. When evaluated using aged oilfield wastewater as a model system, both membrane types demonstrated excellent performance, achieving nearly complete oil removal and approximately 80% turbidity reduction. The film membrane was particularly

Fig. 20 BT-SEM analysis shows the membrane surface before and after wastewater treatment **a** PVA fiber before water filtration, **b** PVA fiber after water filtration, **c** PVA-UFBE nanofiber before water filtration, **d** PVA-UFBE nanofiber after water filtration, **e** PVA film before water filtration, **f** PVA film after water filtration, **g** PVA-UFBE film before water filtration, **h** PVA-UFBE film after water filtration (Yellow arrows show the pollutants accumulation on the surface of the membrane)

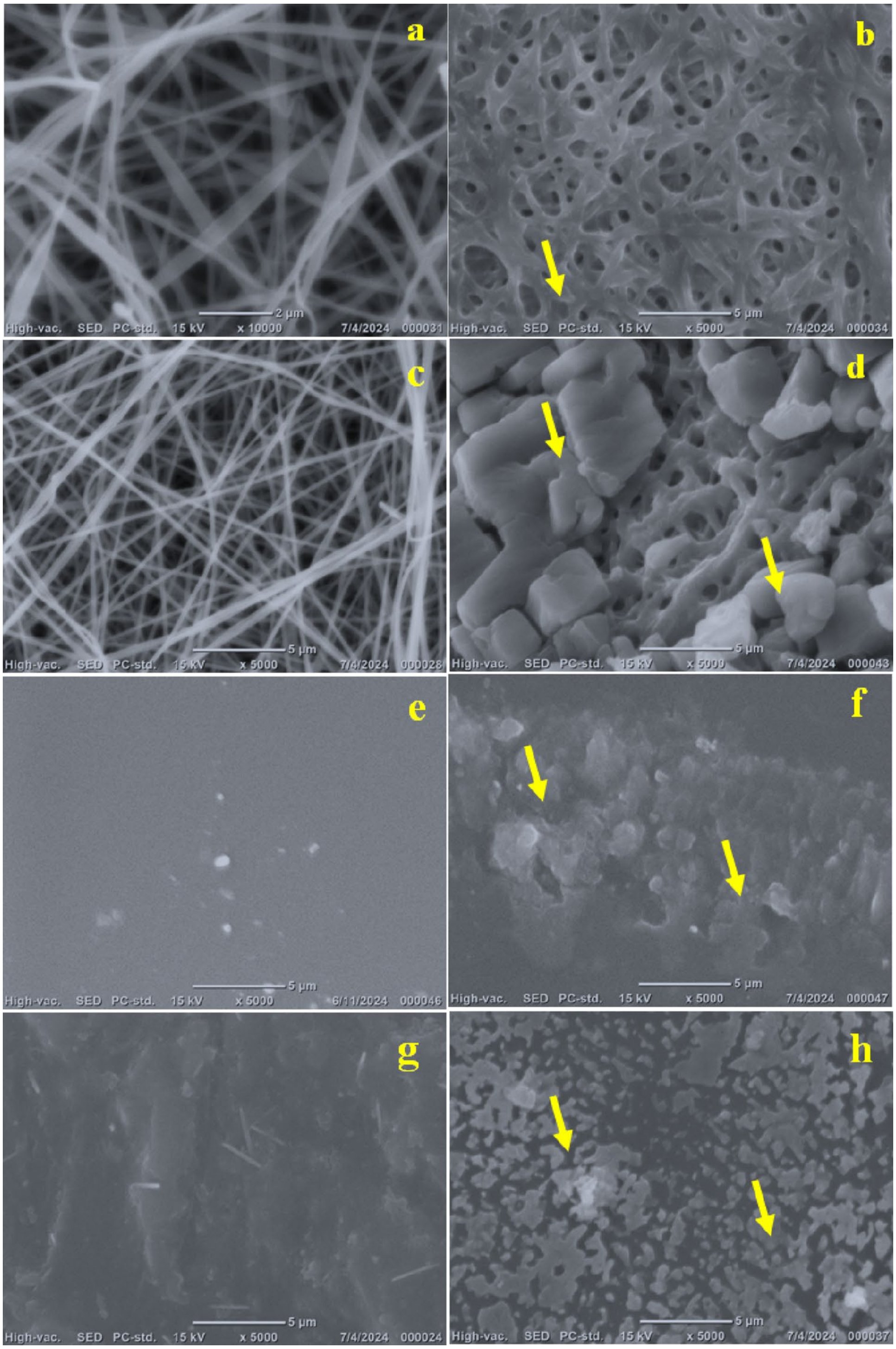

effective in decreasing alkalinity and hardness, while the nanofiber configuration showed superior resistance to mineral scaling, achieving a 76% reduction in scaling tendency. The complementary nature of these functionalities indicates that a hybrid treatment system combining both membrane formats could maximize pollutant removal efficiency across diverse water quality parameters. Overall, this work establishes a foundational platform for the design of multifunctional, bio-derived membranes, offering a novel intersection between material science, biowaste valorization, and environmental engineering for advanced wastewater treatment applications. For future work, composite membranes, such as coaxial PCL-PVA nanofibers, could be designed to enhance mechanical stability and fouling resistance. Additionally, surface modification with antifouling additives may be applied to further reduce foulant adhesion and improve the membrane's surface durability.

Supplementary Information The online version contains supplementary material available at https://doi.org/10.1007/s13201-026-02807-z.

Acknowledgements This work was supported by the Science, Technology & Innovation Funding Authority (STDF), Egypt under the grant number 45614.

Author contributions Conceptualization and supervision were provided by Wael Mamdouh. Shimaa Husien conducted material preparation, data collection, and initial analysis. Waleed I.M. El-Azab and Hager R. Ali performed the water analysis and contributed to its interpretation and discussion. Nour Sh. El-Gendy was responsible for funding the acquisition. The original draft of the manuscript was written by Shimaa Husien, with Waleed I.M. El-Azab and Hager R. Ali contributing to the drafting of the water analysis section and participating in the overall manuscript review and editing. Wael Mamdouh and Nour Sh. El-Gendy provided critical comments and revisions. All authors reviewed and approved the final version of the manuscript.

Funding Open access funding provided by The Science, Technology & Innovation Funding Authority (STDF) in cooperation with The Egyptian Knowledge Bank (EKB). This work was supported by the Science, Technology & Innovation Funding Authority (STDF), Egypt, under Grant No. 45614, awarded to Nour Sh. El-Gendy.

Data availability All relevant data supporting the findings of this study are included within the article and its supplementary materials.

Declarations

Conflict of interest The authors declare that they have no conflict of interests.

Consent for publication Not applicable. This study does not contain any individual person's data or images requiring consent for publication.

Ethical approval Not Applicable. This study did not involve human participants or animal subjects and therefore did not require ethical approval.

References

Abdelhamid AE, Labena A, Mansor ES, Husien S, Moghazy RM (2023) Highly efficient adsorptive membrane for heavy metal removal based on Ulva fasciata biomass. Biomass Convers Biorefinery 13(3):1691–1706

Action S. (2020) World fisheries and aquaculture. Food Agric Organ 2020:1–244

Agüero LEM, Lubambo AF, Saul CK, Silva BF, de Freitas RA, Colodi FG, Duarte MER, Noseda MD (2023) Poly (vinyl alcohol)/ulvan electrospun nanofibers thermallycrosslinked to produce a water stable biomaterial. Biotechnol Res Innov J 7(2):0–0

Aktürk A, Taygun ME, Güler FK, Goller G, Küçükbayrak S (2019) Fabrication of antibacterial polyvinylalcohol nanocomposite mats with soluble starch coated silver nanoparticles. Colloids Surf A 562:255–262

Alwan TJ, Toma ZA, Kudhier MA, Ziadan KM (2016) Preparation and characterization of the PVA nanofibers produced by electrospinning. Madridge J Nanotechnol Nanosci 1(1):1–3

Arumugam N, Chelliapan S, Kamyab H, Thirugnana S, Othman N, Nasri NS (2018) Treatment of wastewater using seaweed: a review. Int J Environ Res Public Health 15(12):2851

Barbieri E, Bondioli ACV (2015) Acute toxicity of ammonia in Pacu fish (Piaractus mesopotamicus, Holmberg, 1887) at different temperatures levels. Aquac Res 46(3):565–571

Baščarević J, Virijević K, Živanović M, Filipović N (2024) The influence of changes in voltage and flow rate on the diameter of electrospun nanofibers. 2024 IEEE 24th International Conference on Bioinformatics and Bioengineering (BIBE), IEEE

Bhardwaj N, Kundu SC (2010) Electrospinning: A fascinating fiber fabrication technique. Biotechnol Adv 28(3):325–347

Boleydei H, Mirghaffari N, Farhadian O (2018) Comparative study on adsorption of crude oil and spent engine oil from seawater and freshwater using algal biomass. Environ Sci Pollut Res 25:21024–21035

Buschmann AH, Camus C, Infante J, Neori A, Israel Á, Hernández-González MC, Pereda SV, Gomez-Pinchetti JL, Golberg A, Tadmor-Shalev N (2017) Seaweed production: overview of the global state of exploitation, farming and emerging research activity. Eur J Phycol 52(4):391–406

Chen J, Zeng W, Gan J, Li Y, Pan Y, Li J, Chen H (2021) Physicochemical properties and anti-oxidation activities of ulvan from Ulva pertusa Kjellm. Algal Res 55:102269

Choo K, Ching YC, Chuah CH, Julai S, Liou N-S (2016) Preparation and characterization of polyvinyl alcohol-chitosan composite films reinforced with cellulose nanofiber. Materials 9(8):644

Deitzel JM, Kleinmeyer J, Harris D, Tan NB (2001) The effect of processing variables on the morphology of electrospun nanofibers and textiles. Polymer 42(1):261–272

Delan WK, Ali IH, Zakaria M, Elsaadany B, Fares AR, ElMeshad AN, Mamdouh W (2022) Investigating the bone regeneration activity of PVA nanofibers scaffolds loaded with simvastatin/chitosan nanoparticles in an induced bone defect rabbit model. Int J Biol Macromol 222:2399–2413

El-Gendy NS, Nassar HN, Ismail AR, Ali HR, Ali BA, Abdelsalam KM, Mubarak M (2023) A Fully Integrated Biorefinery Process for the Valorization of Ulva fasciata into Different Green and Sustainable Value-Added Products. Sustainability 15(9):7319

El-Mahrouk ME, Dewir YH, Hafez YM, El-Banna A, Moghanm FS, El-Ramady H, Mahmood Q, Elbehiry F, Brevik EC (2023) Assessment of bioaccumulation of heavy metals and their ecological risk in sea lettuce (Ulva spp.) along the coast Alexandria, Egypt: Implications for sustainable management. Sustainability, 15(5): 4404

Enayati MS, Behzad T, Sajkiewicz P, Bagheri R, Ghasemi-Mobarakeh L, Łojkowski W, Pahlevanneshan Z, Ahmadi M (2016) Crystallinity study of electrospun poly (vinyl alcohol) nanofibers: effect of electrospinning, filler incorporation, and heat treatment. Iran Polym J 25:647–659

Es-Saheb M, Elzatahry A (2014) Post-Heat Treatment and Mechanical Assessment of Polyvinyl Alcohol Nanofiber Sheet Fabricated by Electrospinning Technique. Int J Polym Sci 2014(1):605938

Garrido-Cardenas JA, Esteban-García B, Agüera A, Sánchez-Pérez JA, Manzano-Agugliaro F (2020) Wastewater treatment by advanced oxidation process and their worldwide research trends. Int J Environ Res Public Health 17(1):170

Greiner A, Wendorff JH (2007) Electrospinning: a fascinating method for the preparation of ultrathin fibers. Angew Chem Int Ed 46(30):5670–5703

Hashim KS, AlKhaddar R, Shaw A, Kot P, Al-Jumeily D, Alwash R, Aljefery MH (2020) Electrocoagulation as an eco-friendly River water treatment method. Advances in Water Resources Engineering and Management: Select Proceedings of TRACE 2018, Springer

Holdt SL, Edwards MD (2014) Cost-effective IMTA: a comparison of the production efficiencies of mussels and seaweed. J Appl Phycol 26:933–945

Huang Z-M, Zhang Y-Z, Kotaki M, Ramakrishna S (2003) A review on polymer nanofibers by electrospinning and their applications in nanocomposites. Compos Sci Technol 63(15):2223–2253

Ibrahim MI, Amer MS, Ibrahim HA, Zaghloul EH (2022) Considerable production of ulvan from Ulva lactuca with special emphasis on its antimicrobial and anti-fouling properties. Appl Biochem Biotechnol 194(7):3097–3118

Jiang J-Q (2015) The role of coagulation in water treatment. Curr Opin Chem Eng 8:36–44

Jipa IM, Stoica A, Stroescu M, Dobre L-M, Dobre T, Jinga S, Tardei C (2012) Potassium sorbate release from poly (vinyl alcohol)-bacterial cellulose films. Chem Pap 66:138–143

Karwasra BL, Gill BS, Kaur M (2017) Rheological and structural properties of starches from different Indian wheat cultivars and their relationships. Int J Food Prop 20(sup1):S1093–S1106

Kim JK, Yarish C, Hwang EK, Park M, Kim Y (2017) Seaweed aquaculture: cultivation technologies. challenges its Ecosyst Serv Algae 32(1):1–13

Ktari L, Chebil Ajjabi L, De Clerck O, Gómez Pinchetti JL, Rebours C (2022) Seaweeds as a promising resource for blue economy development in Tunisia: current state, opportunities, and challenges. J Appl Phycol, 1–17

Kuchaiyaphum P, Punyodom W, Watanesk S, Watanesk R (2013) Composition optimization of polyvinyl alcohol/rice starch/silk fibroin-blended films for improving its eco-friendly packaging properties. J Appl Polym Sci 129(5):2614–2620

Le Van H, Zhai L, Kim HC, Kim J, Kim J (2019) Green Nanocomposites Made With Polyvinyl Alcohol And Cellulose Nanofibers Isolated From Recycled Paper. J Renew Mater 7:621–629

Lee K-H, Kim H, Khil M, Ra Y, Lee D (2003) Characterization of nano-structured poly (ε-caprolactone) nonwoven mats via electrospinning. Polymer 44(4):1287–1294

Lekshmi R, Rejiniemon T, Sathya R, Kuppusamy P, Al-Mekhlafi FA, Wadaan MA, Rajendran P (2022) Adsorption of heavy metals from the aqueous solution using activated biomass from Ulva flexuosa. Chemosphere 306:135479

Liu D, Sun X, Tian H, Maiti S, Ma Z (2013) Effects of cellulose nanofibrils on the structure and properties on PVA nanocomposites. Cellulose 20:2981–2989

Liu Q, Li Y, Chen H, Lu J, Yu G, Möslang M, Zhou Y (2020) Superior adsorption capacity of functionalised straw adsorbent for dyes and heavy-metal ions. J Hazard Mater 382:121040

Madany MA, Abdel-Kareem MS, Al-Oufy AK, Haroun M, Sheweita SA (2021) The biopolymer ulvan from Ulva fasciata: Extraction towards nanofibers fabrication. Int J Biol Macromol 177:401–412

McHugh DJ (2003) A guide to the seaweed industry

Nassar HN, El-Azab WI, El-Gendy NS (2022) Sustainable ecofriendly recruitment of bioethanol fermentation lignocellulosic spent waste biomass for the safe reuse and discharge of petroleum production produced water via biosorption and solid biofuel production. J Hazard Mater 422:126845

Paipitak K, Pornpra T, Mongkontalang P, Techitdheer W, Pecharapa W (2011) Characterization of PVA-chitosan nanofibers prepared by electrospinning. Procedia Eng 8:101–105

Paulert R, Júnior AS, Stadnik MJ, Pizzolatti MG (2007) Antimicrobial properties of extracts from the green seaweed Ulva fasciata Delile against pathogenic bacteria and fungi. Algol Stud 123(1):123–130

Plaza M, Santoyo S, Jaime L, Reina GG-B, Herrero M, Señoráns FJ, Ibáñez E (2010) Screening for bioactive compounds from algae. J Pharm Biomed Anal 51(2):450–455

Ramakrishna S (2005) An introduction to electrospinning and nanofibers. World scientific

Salbitani G, Carfagna S (2021) Ammonium utilization in microalgae: A sustainable method for wastewater treatment. Sustainability 13(2):956

Saleh IA, Zouari N, Al-Ghouti MA (2020) Removal of pesticides from water and wastewater: Chemical, physical and biological treatment approaches. Environ Technol Innov 19:101026

Sarmah AK, Meyer MT, Boxall AB (2006) A global perspective on the use, sales, exposure pathways, occurrence, fate and effects of veterinary antibiotics (VAs) in the environment. Chemosphere 65(5):725–759

Sen PK, Sen PV, Mudgal A, Singh SN, Vyas SK, Davies P (2011) A small scale Multi-effect Distillation (MED) unit for rural micro enterprises. Part I—design fabrication Desalin 279(1):15–26

Shoaib AG, Van H-T, Tran D-T, El Sikaily A, Hassaan MA and A. El Nemr (2024). Green algae Ulva lactuca-derived biochar-sulfur improves the adsorption of methylene blue from water. Sci Rep 14(1): 11583

Siddaiah T, Ojha P, Kumar NOGVR, Ramu C (2018) Structural, optical and thermal characterizations of PVA/MAA: EA polyblend films. Mater Res 21(5):e20170987

Silva FE, Di-Medeiros MCB, Batista KA, Fernandes KF (2013) PVA/polysaccharides blended films: mechanical properties. J Mater 2013(1):413578

Taha E, Nour SA, Mamdouh W, Naguib MJ (2024) Investigating the potential of highly porous zopiclone-loaded 3D electrospun nanofibers for brain targeting via the intranasal route. Int J Pharm 660:124230

Trivedi N, Baghel RS, Bothwell J, Gupta V, Reddy C, Lali AM, Jha B (2016) An integrated process for the extraction of fuel and chemicals from marine macroalgal biomass. Sci Rep 6(1):30728

Yousef R, Qiblawey H, El-Naas MH (2020) Adsorption as a process for produced water treatment: A review. Processes 8(12):1657

Yuan X, Zhang Y, Dong C, Sheng J (2004) Morphology of ultrafine polysulfone fibers prepared by electrospinning. Polym Int 53(11):1704–1710

Zargham S, Bazgir S, Tavakoli A, Rashidi AS, Damerchely R (2012) The effect of flow rate on morphology and deposition area of electrospun nylon 6 nanofiber. J Eng Fibers Fabr 7(4):155892501200700414

Zhang J, Tang C, Kong Q, He M, Lv P, Guo H, Guo Y, Shi X, Gu J (2025) Strong and tough polyvinyl alcohol hydrogels with high intrinsic thermal conductivity. Soft Sci 5(1):NA–NA

Ziabari M, Mottaghitalab V, Haghi AK (2010) A new approach for optimization of electrospun nanofiber formation process. Korean J Chem Eng 27:340–354

Zinicovscaia I (2016) Conventional methods of wastewater treatment. Cyanobacteria Bioremediat wastewaters, 17–25